I -29556

(3.5)

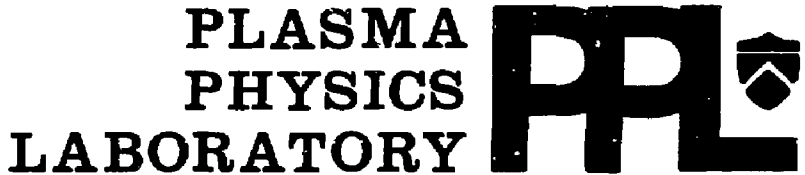# TOKAMAK X-RAY DIAGNOSTIC INSTRUMENTATION

By

K.W. Hill, P. Beiersdorfer, M. Bitter, E. Fredrickson,
S. von Goeler, H. Hsuan, L.C. Johnson, S-L. Liew, K. McGuire,
V. Pare, N.R. Sauthoff, S. Sesnic, and J.E. Stevens

JANUARY 1987

# PLASMA PHYSICS LABORATORY

# PRINCETON UNIVERSITY
## PRINCETON, NEW JERSEY

# TOKAMAK X-RAY DIAGNOSTIC INSTRUMENTATION

K.W. HILL, P. BEIERSDORFER, M. BITTER, E. FREDRICKSON, S. VON GOELER,

H. HSUAN, L.C. JOHNSON, S-L. LIEW, K. MCGUIRE, V. PARE´*, N.R. SAUTHOFF,

S. SESNIC, and J.E. STEVENS

Princeton University, Plasma Physics Laboratory

Princeton, New Jersey

## ABSTRACT

Three classes of x-ray diagnostic instruments enable measurement of a variety of tokamak physics parameters from different features of the x-ray emission spectrum. (1) The soft x-ray (1-50 keV) pulse-height-analysis (PHA) diagnostic measures impurity concentrations from characteristic line intensities and the continuum enhancement, and measures the electron temperature from the continuum slope. Multiple Si(Li) and Ge detectors provide 230 eV FWHM spectral resolution (at 6 keV) and 50 ms time resolution. A hard x-ray (50-500 keV) version of the PHA diagnostic uses NaI scintillators to measure nonthermal and anisotropic electron velocity distributions from the spectral shape and angular distribution of the bremsstrahlung spectrum. (2) The Bragg x-ray crystal spectrometer (XCS) measures the ion temperature and neutral-beam-induced toroidal rotation velocity from the Doppler broadening and wavelength shift, respectively, of spectral lines of medium-Z impurity ions. Impurity charge state distributions, precise wavelengths, and inner-shell excitations and

*recombination rates can also be studied.* X rays *are diffracted and focussed* by a bent crystal onto a position-sensitive detector. The spectral resolving power $E/\Delta E$ is greater than $10^4$ and time resolution is 10 ms. (3) The x-ray imaging system (XIS) measures the spatial structure of rapid fluctuations (0.1-100 kHZ) providing information on MHD phenomena, impurity transport rates, toroidal rotation velocity, plasma position, and the electron temperature profile. It uses an array of silicon surface-barrier diodes which view different chords of the plasma through a common slot aperture and operate in current (as opposed to counting) mode. The effectiveness of shields to protect detectors from fusion-neutron radiation effects has been studied both theoretically and experimentally.

* Oak Ridge National Laboratory, Oak Ridge, TN

## 1.0 INTRODUCTION

X-ray diagnostic instrumentation on tokamaks has long been used to measure a variety of physical parameters of importance to tokamak physics and fusion research. As tokamak plasmas approach the reactor regime with central electron temperatures greater than 6 keV, the intensity of x-ray emission increases and x-ray methods become even better suited to probe the important hot central region. In this paper an overview of x-ray diagnostic methods is presented, with an emphasis on instrumentation and measurement techniques. A companion paper /1/ reviews some recent experimental physics results obtained with x-ray diagnostics from the Tokamak Fusion Test Reactor (TFTR) and other tokamaks. The great versatility of x-ray diagnostic methods is achieved through exploitation of different aspects of the x-ray emission.

First, for example, photon counting x-ray spectrometers called pulse-height analyzers (PHA) /2-4/ provide an overview of the x-ray emission spectrum from 1 to 50 keV with moderate energy resolution (~ 220 eV FWHM at 6 keV) and coarse time resolution (50 ms). These instruments measure impurity concentrations and electron temperature. Higher energy spectrometers in this class, operating in the energy range from 50 to 500 keV, measure the electron distribution function /5/ in the case of nonthermal or suprathermal electron distributions.

Second, Bragg x-ray crystal spectrometers (XCS) /4,6-9/ measure characteristic line radiation from high-Z impurity ions with excellent energy resolution ($E/\Delta E \sim 10^4$) and moderate time resolution (10 ms). This class of instrument measures the impurity ion temperature from Doppler broadening of the impurity x-ray line /7,10/. Other important uses include the measurement of neutral-beam-induced toroidal plasma rotation in tokamaks from the Doppler shift of the lines /11-14/; the measurement of ion charge-state distributions

and the ionization equilibrium /6,11/ from the intensities of x-ray lines from the various charge states of an ion species; precise measurements of wavelengths of x-ray lines /11,15-17/; and measurement of line excitation rates and dielectronic recombination rates /18/. A recent novel application of the XCS is the measurement of the radial profile of neutral hydrogen density in a tokamak from x-ray lines produced through charge exchange or capture of an electron from the hydrogen neutrals /19/.

Third, the x-ray imaging (XIS) system /20,21/ provides an image of rapid fluctuations in the plasma x-ray emission based on analysis of a cross section of the minor radius. Its characteristics are good position resolution, 1-2 centimeters, course energy resolution provided by x-ray filter foils, and excellent time resolution (1 μs). This instrument can also measure a variety of plasma phenomena /22/, including MHD instabilities, determination of the q = 1 radius and plasma position, toroidal plasma rotation velocity, and electron temperature profiles /23,24/.

Instruments in all three classes of x-ray diagnostics can be used to measure impurity transport rates /11,25-28/. A recently developed version of the x-ray imaging system is a pinhole camera with a two-dimensional detector /29/, which provides a tangential view of the plasma in the PBX (Princeton Beta Experiment) tokamak. Initial results from this diagnostic show differences in internal plasma shapes for circular and bean-shaped discharges.

These x-ray diagnostic instruments and measurement techniques have evolved, improved, and matured over the past 15 years, through development and testing on several tokamaks.

An important aspect of the development of x-ray diagnostic instrumentation for TFTR and for future reactors is the effects of radiation on the instruments /30/. Fusion neutrons and gamma rays resulting from the

interaction of the neutrons in the tokamak structure and surrounding building can produce severe noise signals in the detectors and can produce damage in some types of detectors. The TFTR diagnostic development program has stressed the importance of dealing with this problem, and the TFTR environment has provided a unique opportunity to test the effectiveness of shielding and the accuracy of the computational modeling, which has been used to design shielding for the TFTR facility and for individual diagnostics /31/.

In Sec. 2 the origin of x-ray emission in plasmas is discussed. In Secs. 3-6 the x-ray diagnostics instruments are described with examples and figures mostly from TFTR. In Sec. 7, some calculations and measurements of shielding effectiveness and radiation noise characteristics are presented. Future plans for development and improvement of diagnostic instruments to satisfy requirements for TFTR with tritium plasmas and for future reactors are discussed in Sec. 8.

## 2.0  TOKAMAK X-RAY EMISSION CHARACTERISTICS

Each of the different classes of x-ray diagnostic instruments was developed to make use of different aspects of the plasma x-ray emission spectrum. In this section, the x-ray spectral characteristics and the mechanisms for generation of x rays in plasmas are reviewed. A typical spectrum measured by the x-ray PHA viewing a central chord in the horizontal midplane of TFTR is shown in Fig. 1a. Figures 1b and 1c are iron K$\alpha$ spectra recorded with Bragg crystal spectrometers having a resolving power of 1700 and 15,000, respectively. They show that the iron K$\alpha$ peak (in Fig. 1a) is actually composed of a large number of x-ray lines from different charge states of iron (Fig. 1b). The PHA spectrum in Fig. 1a has two main features, a continuum which decreases approximately exponentially with x-ray energy, and

characteristic x-ray peaks from impurities. As discussed below, the impurity concentrations are obtained from the intensities of the characteristic peaks, and the electron temperature is measured from the slope of the continuum spectrum on a semilogarithmic plot. The dashed curve plotted along the measured spectrum is a simulated continuum which is calculated for a typical electron temperature and electron density profile shape in TFTR, and represents a maximum likelihood fit to the measured data.

The continuum spectrum results mainly from bremsstrahlung and radiative recombination. The bremsstrahlung emission occurs when electrons are scattered by either bulk plasma or impurity ions (free-free continuum). The recombination continuum results from radiative capture of free electrons by an ion (free-bound). Detailed discussions of the continuum emission have been presented previously /3,4/. Here a simplified outline of the essential features is given.

The bremsstrahlung radiation rate can be expressed by the equation

$$\frac{dP_{ff}}{dE} = 3 \times 10^{-15} \; n_e n_i z_i^2 T_e^{-1/2} \; \bar{g}_{ff}(T_e, E) \exp\left(\frac{-E}{kT_e}\right) \quad , \tag{1}$$

where $dP/dE$ is the power emitted per unit volume density (keV/cm$^{-3}$/sec) radiated into the photon energy interval $dE$ (keV) by an impurity ion with density $n_i$ and effective charge for free-free collisions $Z_i$. The quantity $n_e$ is the electron density in cm$^{-3}$. $T_e$ and $E$ are the electron temperature and photon energy in keV, $\bar{g}_{ff}$ is the temperature averaged Gaunt factor, which is approximately 1 in most cases. Equation 1 must be summed over all ionic species in the plasma to yield the total bremsstrahlung power.

The expression for the recombination radiation is more complicated and has also been presented previously /3,4/. For this discussion, we simplify the recombination expression to the following /3/:

$$\frac{dP_{fb}}{dE} = (\gamma_i - 1)\frac{dP_{ff}}{dE}$$

which is valid for energies greater than the ionization potential of the ion in question. The parameter $\gamma_i$ represents the enhancement of the continuum radiation over hydrogen bremsstrahlung due to recombination radiation from ion species "i". This factor has been calculated for several ions in the literature /3,4,32/. Typical values of $\gamma$ in the 2-4 keV range of electron temperatures vary from $\lesssim 2$ for fully stripped carbon and oxygen to $\sim 8$-$10$ for a coronal-equilibrium distribution of elements such as chlorine ($Z = 17$) or titanium ($Z = 22$).

The principle of measuring electron temperature from the continuum can be understood from the last term in Eq. (1). If we take $\bar{g}_{ff}$ as independent of energy, then the spectrum of Eqs. (1) and (2), and, therefore, of the total continuum has the shape of a straight line on a semilogarithmic graph of dP/dE vs E. The slope is $-1/T_e$, from which $T_e$ is measured. The slight curvature of the theoretical continuum spectra in Fig. 1 at low energies is due to radial profile effects. The spectrometer line of sight samples not only the hot central plasma but also the outer cooler parts of the plasma where the slope (magnitude) is larger. At high photon energies, however, the emission is dominated by the hot central plasma, and the spectrum is approximately linear with a slope more nearly characteristic of the central electron temperature. The procedure of fitting to the measured continuum a simulated continuum which uses realistic density and temperature profiles usually results in a central temperature measurement which is very close to that measured, e.g., from Thomson scattering.

The intensity I of the line radiation in Fig. 1a can be related to the density of impurity species m, $n_m$ by the equation

$$I = n_e\, n_m\, S_{eff}(T_e) \quad ,$$

where $S_{eff}(T_e)$ is a theoretical effective excitation rate which depends on $T_e$. Since the PHA diagnostic, which measures the spectrum in Fig. 1a, does not resolve different lines from different charge states of a metal, the effective excitation rate $S_{eff}$ is a double sum, first over the various lines j emitted by a given charge state, then over the charge i, weighted according to the fractional abundance $f_i$,

$$S_{eff}(T_e) = \sum_{i,j} f_i\, s_{ij}(T_e) \quad ,$$

where $S_{ij}(T_e)$ is the excitation rate for the single line j. The charge-state distribution $f_i$ is usually calculated according to coronal equilibrium but may be measured or calculated according to other prescriptions if deviations from coronal equilibrium are suspected. Excitation rates $S_{ij}$ for individual charge states and the total effective rate $S_{eff}$ for iron have been calculated by Cowan /4/. Values of $S_{eff}$ for chlorine, titanium, and iron have been presented by Silver /3/. Improved individual and total rates for iron have been compiled by Hill and are illustrated in Fig. 2 /33/. These include calculations from Bely-Dubau /34/ to account for contributions which were omitted in the earlier compilation /4/. These rates are 30-50% higher than the earlier rates, and are in better agreement with the measured continuum enhancement in cases where the enhancement is strongly dominated by metals.

All of the aforementioned effective excitation rates assumed a coronal equilibrium distribution of charge states. Recent observations in TFTR indicate that the distribution can be significantly shifted toward lower charge states in low density discharges in the presence of intense neutral beam heating. The effect is apparently due to the capture of electrons by the highly stripped medium-Z ions from deuterium neutrals. The enhanced charge-exchange rate can produce large deviations from coronal equilibrium and can significantly reduce the effective or charge-state-averaged recombination radiation factor $\bar{\gamma}$ [see Eq. (2)] by reducing the fraction of hydrogenlike and fully stripped species /35/.

The individual lines shown in Fig. 1c result mainly from direct inner-shell impact excitation and dielectronic recombination. Contributions from inner-shell ionization, radiative recombination, and inner-shell excitation to levels $n > 2$ followed by cascading are usually smaller in tokamaks. Calculated rates for these processes in iron are given in Ref. 34. Also methods for calculating the rates and references to calculations by other physicists are given. References 11, 15, and 16 present similar detailed rates for titanium and compare the calculations with measurements. Excitation of x-ray lines by charge transfer from neutral hydrogen to highly stripped impurity ions can become significant under conditions of relatively high neutral density, e.g., near the plasma edge or in the presence of intense neutral beam injection. The small neutral fraction can be offset by the large cross sections for this process ($\sim 10^{-14} cm^2$ for $Ar^{+17}$). The capture usually occurs in high n levels of the impurity ion, but cascading could result in contributions to the inner-shell lines of Fig. 1(c).

### 3.0  X-RAY PULSE-HEIGHT-ANALYSIS DIAGNOSTIC

The x-ray pulse-height-analysis (PHA) system is used to provide an
overview of the overall x-ray spectrum. It uses photon counting detectors
which are sensitive to the photon energy /2-4/. Each x-ray photon generates a
voltage pulse whose amplitude is proportional to the photon energy. The
pulses are sorted and binned according to energy by a pulse-height analyzer,
resulting in a spectrum in which the number of photons is plotted versus x-ray
energy. In the soft x-ray region, 1-100 keV, either lithium-drifted silicon
Si(Li) or high purity germanium (HPGe) detectors are used /30/. At higher
energies (0.1-10 MeV) scintillator crystals, usually NaI, coupled to
photomultiplier tubes are more efficient /5/. The discussion of this section
refers primarily to the soft x-ray PHA system.

The principles of a PHA system which views a single chord of the plasma
are illustrated in Fig. 3. X-ray photons falling onto three or more detectors
are prefiltered by remotely selectable x-ray absorber foils and pairs of fixed
and remotely selectable apertures. The foils select x-ray energy bands, and
the aperture pairs adjust the photon flux or count rate. In general, thin
metal foils are used when $T_e$ is low, and thicker foils are chosen to measure a
spectrum at higher x-ray energies when $T_e$ is large /3/. Similarly, small
diameter apertures are used for high photon fluxes (e.g., high $n_e$, many
impurities), and larger apertures for low fluxes.

Multiple detectors are required because a single photon counting detector
cannot simultaneously satisfy the requirements of good energy resolution, good
time resolution, accuracy of $T_e$ measurement, and the capability to measure a
reasonable range of plasma electron temperatures without changing foils or
apertures /4/. More specifically, an energy resolution of 230 eV FWHM at 6
keV is required to permit separation of the $K\alpha$ x-ray peaks of typical

impurities such as titanium, chromium, iron, and nickel. To attain this energy resolution the pulse width of the pulse shaping amplifiers must be at least 10 microseconds /36/. Second, reliable $T_e$ measurement requires good statistics over an x-ray energy range of 2-5 times $T_e$. As Fig. 1a illustrates, the photon intensity varies by 3 to 4 orders of magnitude in this range. Third, good time resolution (50 ms) requires a net count rate greater than $10^5$ counts/second. At high count rates pulse pileup can distort the spectrum and cause the $T_e$ measurement by a single detector to be unreliable.

Pulse pileup occurs when two simultaneously arriving x rays produce pulses that overlap and result in a single pulse of higher amplitude which is interpreted as a single x ray having an energy equal to the sum of the two individual x-ray energies. Because the x-ray photon count rate is 3-4 orders of magnitude lower at high energies where piled up pulses tend to appear, than at low energies where the relatively higher count rate tends to cause pulse pileup, even a small percentage of piled up pulses can produce an unacceptably high relative distortion of the high energy portion of the spectrum. Thus, the individual detectors in a PHA system are constrained to different bands of the desired spectrum, and the resultant overall spectrum is obtained as a composite of the pieces from the separate detectors. The selection of foils and aperture diameters for various x-ray energy ranges and $T_e$ ranges has been discussed previously /3/.

Each of the three PHA arms on TFTR has six detectors in order to maximize the time resolution and dynamic range within the geometrical constraints imposed by TFTR. The detectors are arranged as two independent triplets in order to accommodate large temperature excursions expected during neutral beam heating; i.e., the filters and apertures for one triplet can be selected for a low $T_e$ range (2-3 keV) as expected before neutral beam heating, and the second

triplet can be independently optimized for a high $T_e$ range (e.g., 6-10 keV) as expected during neutral beam heating.

The data acquisition electronics are configured to provide for 32 time groups of 512 channel spectra at 100 eV/channel or 64 time groups of 256 channel spectra at either 100 or 200 eV/channel. The integration times for the spectra are specified by software in terms of phases, in order to provide maximum flexibility in apportioning the available 32 or 64 time groups to the interesting regions of the shot, which typically lasts 4 - 6 seconds. From 1 to 10 phases can be specified, the ith phase beginning at time $t_i$ and containing $m_i$ time groups of duration $\Delta t_i$. Of course, $\sum m_i$ must be less than or equal to 32 or 64, the total number of time groups available. The time resolution $\Delta t_i$ within a phase can range from 1 ms to 1 sec, and the phases need not be contiguous.

A model is used to infer central plasma parameters from the single-chord PHA spectrum (Fig. 1a). The spectrum is fitted by a simulated, chord-integrated bremsstrahlung spectrum (Eq. 1) which is based on either analytic electron temperature and density profile shapes, or measured profiles from Thomson scattering. Impurity densities are assumed proportional to electron density, as supported by $Z_{eff}$ profile measurements from visible bremsstrahlung. Both the central electron temperature and the continuum enhancement due to impurities (Eq. 2) are inferred from the best-fit spectrum. Metal impurity concentrations are derived from comparison of simulated, chord integrated $K\alpha$ line intensities, based on Eqs. (3) and (4), to measured intensities. The low-Z impurity concentration is derived from two equations which express (1) charge neutrality and (2) the total continuum enhancement due to the known metals and the unknown low-Z impurity density. The low-Z impurities are assumed to be carbon and oxygen in a ratio of 3:1 to 8:1, as inferred from UV spectroscopy.

### 4.0  X-RAY CRYSTAL SPECTROMETERS

High resolution x-ray crystal spectrometry has evolved over the last decade into a powerful diagnostic of several plasma parameters /6-16/. The crystal spectrometer instrument is used to make time-dependent measurements of characteristic x-ray lines of highly stripped impurity ions in the plasma with good energy resolution (resolving power $\lambda/\Delta\lambda$ = 10,000-25,000). The strength of this technique lies in the fact that the inner shell excitations probe the hot central core of the plasma, while extremely good wavelength or energy resolution permits good separation of individual inner shell transitions as well as measurement of x-ray line shapes.

The measurement of ion temperature $T_i$ by Doppler broadening of impurity lines and the determination of the plasma bulk motion due to neutral-beam-driven toroidal rotation have been the major reasons for the development of this diagnostic in tokamaks. Nevertheless, its capability to measure a variety of other plasma parameters, including the electron temperature, impurity transport rates /11/ and charge-state distributions /6-11/, and neutral hydrogen density /19/ has been demonstrated. Some of the most significant contributions of high resolution x-ray spectrometry on tokamaks have been in the field of atomic physics /11,15-19/. These include very precise measurements of wavelengths of x-ray lines from highly stripped medium- to high-Z ions, and measurement of relative line intensities, which yield information on excitation and recombination processes and their rate coefficients. These measurements are made possible by the excellent energy resolution of the XCS coupled with the unique capabilities of the tokamak to produce highly stripped medium- and high-Z ions in a steady state and a relatively collisionless regime.

Since excellent papers on the details of x-ray crystal spectrometer requirements and design exist /6,9,10/, this paper will present mainly an overview of the basic design philosophy, requirements, and considerations. The main requirement of the XCS is high energy resolution. A resolving power of $10^4$ is required to measure $T_i$ from Doppler broadening, since the Doppler broadening $\Delta\lambda$ is typically 3-5 x $10^{-4}$ $\lambda$. This type of energy resolution is not possible with energy dispersive detectors such as Si(Li) or proportional counters, but is realizable through Bragg diffraction. This fact is demonstrated by the contrast between the low resolution PHA spectrum in Fig. 1a and the XCS spectra in Figs. 1b and 1c of iron measured with resolving powers of 1700 and 15,000, respectively.

The principal features of the Johann XCS are illustrated schematically in Fig. 4. The plasma x rays pass through a beryllium window and are Bragg reflected from the crystal to the detector. The instrument involves four essential ingredients. First, the Bragg condition $n\lambda = 2d \sin\theta$ must be satisfied in order for x rays to be diffracted. Here n is the order of diffraction, $\lambda$ the wavelength, 2d the crystal lattice spacing, and $\theta$ the angle of incidence and exit. Secondly, if the crystal is cylindrically curved to a radius R, x rays from or passing through a point on a Rowland circle of diameter R will all strike the crystal at the same angle $\theta$. Thus, if the wavelength and angle satisfy the Bragg condition, all of these x rays will be diffracted by symmetry to another point on the Rowland circle. The detector is located at this point. Third, the plasma region selected is a homogeneously emitting extended source. Thus the selection of different x-ray wavelengths by the crystal from different parts of the plasma will not change the x-ray spectrum. Fourth, a position sensitive detector is used to collect the x rays. Thus, a position on the detector is equivalent to wavelength.

Other important ingredients are either a helium path or a vacuum path to minimize absorption by the air, and shielding such as polyethylene and lead around the detector to minimize noise from neutrons, gamma rays, and hard x rays.

X-ray crystal spectrometry at Princeton has evolved over the last decade from the simple scanning monochromator used on the ST tokamak /37/ to the very high resolution polychromators used on PLT and PDX, and to the multichord polychromator array now used on TFTR /30,38/. The first major advance was use of a position-sensitive multiwire proportional counter /6/, which permitted simultaneous measurement of the full $K\alpha$ spectrum of all charge states of iron, i.e., an energy range of 300 eV, and recording of four spectra during a shot for time resolution. The energy resolving power was 1700. A measurement of the charge-state distribution of iron versus electron temperature showed that the distribution satisfied coronal equilibrium within the theoretical uncertainties. The next advance was development of an instrument with a resolving power of 15,000 to permit ion temperature measurement from Doppler broadening of the helium-like $K\alpha$ resonance line of iron /10/. With this instrument an ion impurity temperature up to 7.0 keV was measured on PLT with 4 MW of neutral beam heating. A similar instrument was installed on PDX, measuring the heliumlike and hydrogenlike titanium $K\alpha$ spectrum /12,16/. Since its line of sight had a tangential component, the neutral-beam-induced toroidal rotation velocity could be measured from the Doppler shift of the titanium XXI $K\alpha$ resonance line.

The TFTR x-ray crystal spectrometry system consists of one horizontal instrument viewing the central midplane of the plasma /7,11/ and a vertical system with three spectrometers /30,38/ which view three chords of the plasma vertically. The vertical system views the plasma at major radii R = 2.25,

2.45, and 2.95 m. The plasma center ranges from R = 2.45 m to R = 2.58 m for a minor radius a = 0.82 m. Major improvements leading to these T FTR systems /30/ include development of multiwire proportional counters /39/ which can handle count rates greater than $3.5 \times 10^5 \text{ s}^{-1}$ without degradation of resolution or pulse height (10 times higher than the capability of the original PLT system), use of a time-to-digital converter for approximately 10 times higher throughput than the original time-to-amplitude converter/analog-to-digital converters used on PLT, and use of more memory for 128 time groups during a shot. The higher x-ray emissivity and better throughput permits time resolution as small as 10-20 ms.

The spectrometers at Princeton have generally had a long focal length (3 m for PLT to 10 m for the TFTR vertical system), and are hence bulky and cumbersome to readjust to other spectral bands. This size is motivated mainly by the high resolving power required for Doppler-broadening measurements and the limited detector position resolution of 0.2-0.3 mm FWHM. However, the larger size of the TFTR vertical system as well as the system on the JET tokamak is due also to geometrical restrictions. The crystal and detector portions of these systems are located far from the tokamak and beyond concrete walls to reduce radiation levels. The very long focal lengths are required to keep the focal point near the tokamak and thus minimize the length of the beryllium window.

To achieve a resolving power of $10^4$ a crystal must have the necessary 2d spacing, good inherent resolving power or a narrow rocking curve, and precision curvature. Usually one of several diffraction planes of quartz crystals is suitable for the Kα lines of elements such as Ti, Cr, Fe, or Ni /40,41/. The crystal plate must have very flat front and back surfaces which are highly parallel to each other and also parallel to the crystal plane to be

used. Once the crystal plate is curved, the permitted deviation of the front surface from a cylinder is about 1 μm.

Often compromises must be considered in designing an XCS for tokamaks. First, a large Bragg angle θ generally gives better resolution and reflectivity, but results in a smaller wavelength range. The energy resolution is better both because the dispersion $d\theta/d\lambda$ is larger and because the detector is more nearly tangent to the Rowland circle. A second choice involves detector type. The multiwire proportional counter can have high efficiency, excellent uniformity, and count rates ~ $5 \times 10^5$ with moderate position resolution (~ 0.2 mm FWHM). However, because of the depth of the gas volume (~ 5-20 mm), it must be perpendicular to the x-ray beam from the crystal, and thus cannot be precisely tangent to the Rowland circle at all points of its active length. Other detectors such as microchannel plate intensifiers have better position resolution and count rate capability because they can be operated in a current mode also. They can also be placed at an angle to the incoming x-ray beam, and thus can be placed more nearly tangent to the Rowland circle. However, the x-ray efficiency is low, usually much less than 10%, and the uniformity along the detector surface is much poorer than that of the multiwire proportional counter.

Figure 1c illustrates a typical Kα spectrum of mostly heliumlike iron measured, in this case, from PLT with an XCS having a resolving power of 15,000. This good spectral resolution allows separation and identification of spectral features, and good measurement of line shapes. The labels on the peaks are taken from Gabriel /42/. The line labelled "w", which results from the 1s-2p resonance transition in heliumlike iron, is the line usually used for measurement of ion temperature. This line is convenient because it is relatively free of features on the short wavelength side and in the region

between d13 and x.    Examples of these measurements are discussed in the references /1,7,10,11/.

## 5.0  THE X-RAY IMAGING SYSTEM

The concept of the x-ray imaging system (XIS) is illustrated schematically in Fig. 5, which shows the horizontal XIS on TFTR /20/.   For this system 76 silicon surface barrier (SB) diodes lying on a circular arc view the plasma through a common slot aperture.   Thus, different detectors sample the plasma x-ray emission integrated across different chords of the minor cross section at a fixed toroidal location.   The main purpose of the XIS is to measure the spatial structure of rapid fluctuations in the plasma x-ray emission and, thereby, provide information on the plasma instabilities that cause the fluctuations /20,22/.   The modulation in emission may result from MHD activity, from the outward propagation of a heat pulse resulting from an internal disruption /43/, or from the motion of impurities injected into the plasma /27,28/.   The latter two examples provide information on thermal transport and impurity transport times.   Other uses for the XIS include measurement of plasma position, position of the q=1 radius, and beam-induced toroidal rotation velocity.

The principle of operation of the XIS is simple.   X rays striking the detector generate a current which is amplified, digitized, and stored to produce a time series for later display and analysis.   The detector and aperture area and foil thickness are chosen to yield a current of $\sim 1\,\mu A$ for the central detector.   The filter thickness is selected to result in a monotonic decrease in signal level with minor radius.   This radial gradient in emissivity serves to provide some effective spatial localization of the line-integral signal, thereby enhancing the ability to analyze radial changes in

the profile shape (sawteeth) or rotation of a non-axisymmetric emissivity profile about the plasma axis (m=1 activity). Poloidal and toroidal variations in the plasma structure are often described in terms of harmonics of the form $\exp(im\theta \pm in\phi)$, where $\theta$ is the poloidal angle, $\phi$ the toroidal angle, and m and n are integers. Both the aperture and detectors are usually rectangular with the long dimension extending toroidally to maximize signal strength and the short dimension running perpendicular to the minor axis and chosen to provide a position resolution of 3-5% of the plasma minor radius.

The digitization is performed at two rates: a slow rate which spans the full discharge duration and a fast rate (from 1 kHz to 1 MHz, depending on the frequency of the fluctuations of interest). For plasma impurity transport studies special filter materials and thicknesses may be used to select characteristic K or L lines of particular impurity charge states to facilitate easy identification of the behavior of these states.

The principle of operation of the XIS may be visualized more graphically from Fig. 6. This figure demonstrates a model which attempts to simulate the experimental m=1,n=1 emissivity profile of Fig. 6d. The circular structure in Fig. 6a represents the plasma minor cross section. The various traces in Fig. 6c represent the time behavior of signals from XIS detectors which view different chords of the plasma. The circles in the plasma cross section (Fig. 6a) are contours of equal x-ray emissivity which generally decrease in amplitude from the center to the edge (Fig. 6b). The shaded region represents a magnetic island at the q=1 radius with m=1, n=1 structure. The effect of the magnetic island is to flatten the x-ray emissivity profile inside the shaded area, as shown in Fig. 6b. Note also that the central set of circles is displaced to the right of the plasma geometric center. This shift results in an off-center peak of increased emissivity with a ledge of constant

emissivity on one side. As the island structure and peak rotate about the center, they modulate the emission seen by the detectors which view inside the q=1 radius. These perturbations are typically 5-10% of the dc level.

Three properties of the emission are noticed: (1) The oscillations below the center are 180° out of phase relative to those above the center, as expected. (2) The central oscillations have twice the frequency of the outer-channel oscillations; this is because the hot spot or high emissivity peak passes the central detector twice during one rotation of the island. It can be seen that the model reproduces the main features of the measured fluctuations. One complication is that the detectors view chordally integrated emission rather than local emission. Thus the line-of-sight profiles have less distinct features than the local profiles. Secondly, the poloidal resolution of each detector is comparable to the separation of neighboring detectors, thus broadening the features somewhat. (3) The time duration of the signal spike increases as we go from outer radii toward the center. This is because inner detectors view the high intensity peak for a longer period of time.

## 6.0 HARD X-RAY PULSE-HEIGHT SPECTROMETER

The hard x-ray spectrometer measurement of the hard x-ray bremsstrahlung emission from the plasma can yield information on anisotropic non-Maxwellian electron distributions /5/. This is especially important in lower hybrid current drive (LHCD) experiments, where the plasma current is carried by an energetic electron tail of the electron distribution which is driven by rf-excited lower hybrid waves. The measurement of the electron distribution function can elucidate the processes of wave interaction with the plasma, which is important in developing and improving the LHCD technique. In this

section the instrumentation and some of the data interpretation and modeling techniques are discussed /44/.

The concept of the measurement of anisotropic non-Maxwellian distribution functions from the x-ray emission relies on the fact that for electron energies greater than 20 keV the bremsstrahlung is significantly peaked in the forward direction, i.e., the direction of motion of the electron. This is illustrated in Fig. 7. Thus a detector which is collimated to accept photons which propagate parallel to the magnetic field will respond more to parallel electrons than will a detector which views perpendicular to the magnetic field, and vice-versa. This measurement is not simple, however, even with spectrally resolved measurements as a function of angle to the magnetic field. This is because the electrons in the plasma have a range of energies and directions, and any electron can emit a photon of lower energy in any direction. Thus, not only must the spectra be measured as a function of angle, but also calculations of the emission from model electron distributions must be done to permit a confident inference of the most likely distribution function. The measurement is further complicated by the fact that the plasma hard x-ray emission is usually much less intense than emission from the limiter and walls due to runaway electron impact, and often there can be neutron- and gamma-induced noise in the detector.

The instruments for measuring the electron distribution function during LHCD experiments on PLT have been described by von Goeler /5,45/. Here the equipment and measurement concept will be briefly reviewed. The main instrument is illustrated in Fig. 8. The x-ray spectra are measured by a 3-in diameter by 3-in long NaI scintillator-photomultiplier. The scintillator is large enough to absorb the Compton-scattered photons and thus to provide nearly 100% photopeak efficiency for x-ray energies up to 850 keV. A 10-in-

thick Pb shield prevents noise from the hard x-ray background. A system of apertures constrains the view to a line such that x rays entering the detector can come from only one direction. The direction of view is selectable by rotating the instrument about a pivot point from nearly forward or parallel emission at $\theta$ = 28 degrees to perpendicular viewing at $\theta$ = 86 degrees, where $\theta$ is the angle between the line of sight and the magnetic field. For angles greater than 90 degrees, the plasma current and magnetic field are reversed.

To ensure that the detector system was responding to x-ray emission from the plasma and not wall radiation, the spectra at $\theta$ = 86 degrees were compared with spectra from a vertically viewing hard x-ray detector system. The two spectra were identical. It is believed that the vertical hard x-ray system responds only to plasma radiation and not to radiation from the wall or scattered from other structural members since the detector is tightly constrained to avoid viewing the pipes or the wall, and views only a beryllium window which is recessed 46 centimeters from the vacuum vessel into the wedge casting of the tokamak torque frame. This viewing dump ensures that the detectors will not view wall radiation or scattered radiation. Data from the vertical hard x-ray system were also used to normalize spectra from the tangential system to correct for small changes in the current drive characteristics when the magnetic field, plasma current, and waveguide phasing were reversed for measurement of the backward x-ray emission. Further confidence that plasma radiation dominates the spectra measured by the tangential system was derived from impurity injection experiments during which the x-ray emission intensity increase and time behavior were consistent with those expected from the increase in $Z_{eff}$ due to the impurities. An estimate of the effective path length of the hard x-ray emitting region as a function of viewing angle $\theta$ was derived from the perpendicular viewing soft x-ray

PHA. This diagnostic can be scanned to measure different chords of the plasma minor cross section and measures a hard x-ray tail in the 12 - 25 keV region. Abel-inverted x-ray intensities from radial scans provided geometrical correction factors for the tangentially viewing system.

A typical x-ray spectrum from the tangentially viewing system at $\theta = 28$ degrees during LHCD is illustrated in Fig. 9. The spectrum has been fitted with a sum of the two indicated exponentials, which are characterized by "temperatures" of 39 and 84 keV.

As mentioned previously, due to the complexity of the x-ray emission processes, interpretation of the data requires comparison with simulations using a model electron distribution function /44/. The complexities arise because of (1) the variation of emission intensity with electron kinetic energy and direction, and with photon energy and direction; (2) the variation of path length with viewing angle; and (3) probable variations in the electron distribution with minor radius. The modeling was done in terms of a 3-temperature electron distribution function and a maximum electron cutoff energy $E_m$,

$$
f(\vec{p}) = \left\{
\begin{array}{ll}
C_N \exp\left(-\dfrac{p^2}{2T_\perp} - \dfrac{p_\parallel^2}{2T_{\parallel *}}\right) & p_\parallel < p_m \\[4ex]
0 & p_\parallel,\ p > p_m
\end{array}
\right.
$$

where the asterisk represents F for "forward" when $p_\parallel > 0$, and represents B for "backward" when $p_\parallel < 0$. The $p_\parallel$ and $p_\perp$ represent the electron momenta, and $T_{\parallel F}$, $T_{\parallel B}$, and $T_\perp$ are, respectively, temperatures for the forward, backward, and perpendicular directions. The maximum electron energy $E_m^2 = p_m^2 c^2 + m_o^2 c^4$ was used to simulate a high energy limit to the distribution function which

could result from a maximum wave phase velocity due to the lower hybrid wave accessibility condition. Line-of-sight integrations were done to account for changes in geometry with the orientation of the diagnostic. This permitted a direct comparison of the calculated emission with the measurement.

In trying to select parameters which will produce agreement between the calculated and measured emission, it is useful to know how the emission should change as the free parameters are varied. The sensitivity of emission to changes in values of $T_{\|F}$, $T_{\|B}$, and $T_{\perp}$ is illustrated in Fig. 10 for two values of photon energy, 100 and 300 keV. These simulated curves verify the expected result. For example, consider the lower triplet of curves which represent the x-ray emission at 300 keV. The lower solid curve corresponds to $T_{\|F} = 750$ keV, $T_{\perp} = 150$ keV, and $T_{\|B} = 150$ keV. The dot-dashed curve shows that the maximum change in emission when the forward parallel temperature $T_{\|F}$ is increased to 1125 keV or reduced to 375 keV occurs at 0 degrees or in the forward direction. Similarly, the perpendicular viewing detector near 60-120 degrees has the greatest sensitivity to changes in $T_{\perp}$ (reduction to 75 keV or increase to 225 keV), and the backward viewing detector at 150 - 180 degrees responds most to changes in $T_{\|B}$.

## 7.0 RADIATION EFFECTS AND SHIELDING REQUIREMENTS

As tokamaks become more successful in confining and heating particles, the fusion rate increases. Thus the flux of neutrons and accompanying gamma rays and the background noise in detectors increase. The TFTR neutron production rate or source strength has been as high 9 x $10^{15}$ neutrons/sec. The x-ray diagnostic detectors are particularly sensitive to the gamma rays, and to a lesser extent to the neutrons. The noise levels became high even on PLT with neutral beam injection, and the PHA and XCS detectors had to be

shielded. Also, some of the x-ray detectors, the Si(Li) and silicon surface barrier diodes, can be damaged by a high neutron fluence, and the shielding serves to reduce this problem. Thus a significant emphasis of the TFTR x-ray diagnostic development program has been development of shielding to mitigate the radiation effects /30/. Also, TFTR has provided a unique environment to test these transport calculations.

The shielding requirements for the x ray diagnostic detectors are based on an estimate of the background level which is acceptable, i.e., which will not seriously degrade the quality of the measurement, and a prediction of the maximum expected neutron and gamma-ray fluxes and spectral distributions at the diagnostic. The acceptable background noise is different for each of the different detector types. The radiation spectrum incident onto the shield was derived from a model which treated the neutron source geometry and spectrum as well as (n, γ) reactions and scattering in the tokamak structure, walls, ceilings, and floor /46/.

Both the rate of radiation-induced noise pulses in the detector and the distribution of pulse heights are important. This is true even for the XIS detectors, the signal of which is normally integrated to yield current level. Since the bandwidth is usually large, frequent large pulses can produce a level of "spikes" on the traces which can mask high frequency fluctuation levels of interest. Although the PHA and XCS electronics reject, some of the noise due to pulse-height discrimination, unfortunately a large fraction (30-60%) of noise pulses fall within the window of interest and distort the continuum spectral shape or reduce the ratio of signal to background.

Both neutrons and gamma rays tend to produce a broad pulse-height spectrum, decreasing with pulse height. In the case of neutrons in silicon,

for example, most of the pulses result from energy deposition by recoiling silicon atoms due to elastic and inelastic scattering of the neutron. In the case of gamma rays, the pulses are mostly produced by recoil electrons from Compton scattering, which both have a range of energies and may deposit only a fraction of the energy before escaping from the detector. Both effects contribute to noise in the soft x-ray range.

For the FHA detectors, the gamma-generated pulse-height spectrum normally extends to higher energy than that from the continuum x rays and produces a spectrum with a slope whose magnitude is smaller than that of the x-ray continuum. This causes an overestimate of the electron temperature. Even a few thousand counts per second can degrade the $Z_{eff}$ measurement since determination of the low-Z impurity concentration is very sensitive to temperature.

The XCS detector, which can operate at rates greater than $\sim 5 \times 10^5$ counts/sec, can tolerate background levels of one to a few times $10^5 s^{-1}$ with only minor degradation of the ion temperature measurement. This is because the x-ray peaks fall within a narrow band on the detector, whereas background radiation is uniformly distributed. At low rates the noise generates a uniform background under the spectral lines. A uniform background itself does not broaden the x-ray spectral peak, so $T_i$ can still be measured. It does, however, reduce the peak to background ratio and, because of throughput limitations, reduces the rate of x-ray pulses which can get through the electronics. However, at higher rates a significant distortion of the underlying gamma-ray-induced background occurs. The pulses tends to pile up toward one end of the position spectrum and make the choice of background subtraction more difficult.

To understand this phenomena one must understand the principle of operation of the detector. Any x-ray or gamma-ray photon striking some point on the detector results in an electronic pulse which propagates from that position toward both ends of a delay line. One pulse (the "start" pulse) triggers a counter or timer, and the second pulse turns it off ("stop"). The time delay is proportional to the position at which the photon struck the detector. If the photon rate is high, occasionally a second photon will strike nearer to the "stop" end of the delay line than the position of the pulse from the first photon. Thus, its pulse arrives at the "stop" end of the delay line sooner than that of the first pulse, and it turns off the counter too soon. The result is interpreted as a single photon striking closer to the "start" end of the counter than did either of the two photons.

Specification of the tolerable background noise in XIS detectors is more complicated since it depends on the type of measurement being done: (a) studies of sawteeth with ten's of ms period; (b) MHD phenomena with few kHz frequency; or (c) high frequency fluctuations (> 20 kHz). Furthermore the x-ray signal strength typically varies from ~ 1 μA for central chords to ~ 10 nA near the edge, whereas the radiation background is expected to be approximately uniform across the detector array.

For sawtooth studies the 300 Hz filtering used on XIS data effectively suppresses the radiation spikes. Thus an average radiation background current of 10 nA should be tolerable. It might invalidate some data near the plasma edge and result in some loss of information on heat-pulse propagation. A background level of 100 nA, however, would severely degrade the data. For higher frequency studies (b and c above) wider bandwidth filtering (40 - 600 kHz) is used, and the larger radiation background pulses become visible. Fortunately, the random background pulses have a flat frequency-domain

spectral density, whereas the MHD phenomena are often concentrated within narrow frequency bands. Thus, Fourier analysis of the data should help to extract information from the noise. A comparison of spectral power densities of x-ray and background signals led to the conclusions that (1) high frequency fluctuation studies would become impossible at a background current much above 1 nA, whereas (2) MHD oscillations would be clearly visible at a background level of 10 nA, and would even be visible at 100 nA, though mode studies might not be possible.

The detector shielding requirements were based on computer calculations for various combinations of neutron and gamma-ray shielding materials. The materials consisted of two types, a neutron attenuator and moderator, and a gamma-ray attenuator. The neutron moderator is typically a hydrogen-containing material such as borated polyethylene, water-extended polyester (WEP), paraffin, or concrete. The gamma attenuator is usually a single layer of lead inside the neutron shield to attenuate both the incident gamma rays and those produced by neutron capture in the neutron shield or the boron. Both one-dimensional slab model (ANISN) /47/ or spherical model /31/, and three-dimensional calculations were done./31/ Total neutron or gamma ray interaction cross sections were used to predict the background count rate. For the XIS detectors some measured curves of ionization response were used to predict the noise current /48/. Also, some work was done with a detector-response computer code /49/ which predicted pulse-height distributions due to neutrons, gamma rays, and charged particles.

Figure 11 shows typical calculations and measurements of the radiation background noise current in the horizontal XIS detectors inside the test cell. These points have been normalized to unity TFTR neutron source strength, i.e., divided by the total number of neutrons emitted per second.

Most of the earlier calculations were done with a one-dimensional code in order to predict the optimum mix of polyethylene and lead. As the neutron flux became high enough to produce a measurable signal, the measured point at 2.5 cm of lead was obtained. Also, at this time a full three-dimensional calculation was done. The noise predicted by this calculation was much nearer to the measured noise and significantly lower than the results of the one-dimensional calculations.

Figure 12 summarizes some predictions and measurements of radiation-generated background counts versus shield thickness in the PHA Si(Li) detectors, located in the TFTR test cell. Measurements were made with a 10-cm lead shield and with this shield surrounded by 15-20 cm of borated polyethylene (PE). The count rate was normalized to the total TFTR neutron production rate or source strength. The triangles represent calculations in a one-dimensional slab geometry using the ANISN transport code. The points from 0 to 16 cm refer to a lead shield only. Those beyond 16 cm are for a 16 cm lead shield inside a 5% (by weight) borated polyethylene shield. The dashed curve to the left was obtained by shifting the solid curve to the left until it intersects the 10-cm Pb point. This was done for comparison with the measured data, since no ANISN calculations had been done for 10-cm Pb plus polyethylene. The squares refer to one-dimensional spherical calculations. The apparent saturation of shielding effectiveness near 40 cm results from an assumed ~ 2% component of 14 MeV neutrons included with the 2.5 MeV DD neutrons. For the measured points the error bars on shield thickness indicate that the thickness was not uniform. The lead shield was 10-cm thick in front (facing the tokamak) and around the sides, but only 5-cm thick on top, and gaps existed at the liquid nitrogen dewar location. Also the 1% borated polyethylene shield was 20-cm thick in the front and 15-cm thick on the sides.

The radiation background levels measured in the horizontal PHA and XIS are lower than those predicted by the one-dimensional transport codes. This is both encouraging and not completely unexpected. Two main reasons come to mind. First, the one-dimensional codes cannot properly treat the three-dimensional nature of the geometry; in reality the radiation flux density on the sides and, particularly, the back of the shield and detector is lower in both magnitude and average energy than the frontal (facing the tokamak) flux density. The sources for the one-dimensional transport calculations, however, were conservatively taken to be the frontal flux density or radiation current density. Secondly, the PHA electronics has a discriminator which rejects pulses smaller than 2-3 keV equivalent electron energy. The calculations, however, count every pulse, no matter how small. Both measurements and calculations show that a significant fraction of pulses from neutron scattering or Compton scattering of gamma rays can be small, since they result from distant, small angle collisions. The neutron pulse-height spectrum, in particular, is softened by the fact that only a fraction of the energy of recoiling Si or Ge atoms goes into ionization.

At full power, with 27 MW of 120 keV deuterium neutral beams injected into a deuterium plasma, TFTR is expected to produce up to $10^{17}$ neutrons/sec. This is ten times higher than the levels achieved so far. The shielding requirements for the x-ray diagnostics during this phase of operation were determined from the previously discussed acceptable background levels and the data of Figs. 11 and 12.

Since a shield for the PHA located in the test cell would have to be greater than 1-m thick, the diagnostic was relocated outside the test cell's 2-m-thick concrete wall. A 5-cm-diameter vacuum tube penetrates the wall and couples to a 10-cm tube which provides a line of sight to TFTR. No

additional shielding should be required around the PHA detector. The desired 30-cm-thick shield for the horizontal XIS is not possible due to interference from other hardware near the tokamak. Thus, a shield of 7.5 cm of Pb and 15 cm of 1% borated polyethylene has been installed. This should limit the background to $\sim 50$ nA. Only loss of information on high frequency fluctuations (> 20 kHz) and some degradation of information on heat-pulse propagation should be incurred at this level.

Also radiation background information from the XCS detectors has been obtained. The background in the horizontal XCS detector in the test cell becomes intolerable for a neutron source strength greater than $10^{13}$ neutrons/second, even with the existing shield of 10-15 cm Pb surrounded by 15-20 cm of borated polyethylene. Some noise measurements in the vertical XCS detectors located in the diagnostic basement area indicate a measured response of $5 \times 10^{-11}$ counts/neutron. This extrapolates to a true response of $\sim 1.5 \times 10^{-10}$ counts/neutron, since the pulse-height window accepts an estimated 30% of the gamma-ray pulses. Comparison of the measured response with model calculations suggests an average response of 0.5 counts/$\gamma$/cm$^2$ and 0.1 counts/neutron/cm$^2$ in the 10 x 18 cm$^2$ detector. Based on this response, a shield consisting of 10 cm of Pb inside 12 cm of borated paraffin is being designed for full power operation.

## 8.0 FUTURE PLANS

Some additional x-ray diagnostic instruments have been added to TFTR to improve the diagnostic capabilities. A vertically viewing XIS camera with foils matching those on the horizontal XIS has been installed to permit x-ray tomography and measurement of the plasma radial position /50/. Also, two additional vertically viewing PHA arms have been installed in the diagnostic

basement. Along with the horizontal PHA, these should provide three points on the radial profile of impurity concentration, $Z_{eff}$, and $T_e$. The locations are at major radii of 1.94 m and 3.0 m. The plasma centerline is normally R = 2.45 m for large plasmas with minor radius a = 0.82 m. One arm, at R = 1.94 m, has just become operational. The second will be aligned and integrated to TFTR as access permits.

The present x-ray diagnostics, with shielding which is being added, should operate successfully through the DD equivalent breakeven period. For tritium plasmas (DT) in 1988-1989, however, the neutron source strength will be 100 times higher ($\sim 6 \times 10^{18}$ neutrons/sec), and the 14 MeV neutrons will be more penetrating. The present XIS concept has no hope of operating under these conditions due to the high radiation background. To solve this problem a prototype instrument /51/ is being designed to use layered synthetic microstructures (LSM) /52/ or man-made Bragg diffractors to deflect the x-ray beam and thus permit removal of the detector from the line-of-sight neutrons. The LSM is being used because it has a relatively high reflectivity. For higher energy x rays either LiF or pyrolytic graphite crystals might also be used. This instrument will be tested on TFTR in 1987. If the x-ray signal strength is high enough, as calculations suggest, this instrument could provide an approach for monitoring MHD activity in reactors.

Also advancements have been made in low energy x-ray spectroscopy. A small vacuum XCS has been built and installed on PLT. Initial results suggest that this instrument can measure its full spectral range with a much higher throughput (approximately a factor of $10^3$) than the rotating crystal spectrometer used earlier /53/, and has a much better time resolution and larger wavelength range and dynamic range than the large XCS instruments used

for ion temperature measurement and for measuring the neonlike silver spectra /17/. The Rowland circle diameter is 0.57 m. A 10-cm chevron microchannel plate with fiber-optic bundles leading to two end-to-end Reticon self-scanning diode arrays provides good position resolution and a large dynamic range. The spectral resolving power with an ADP crystal at $\lambda = 8.0$ Å is 3000. Higher resolving power should be achievable with slight modifications. Good spectra of Ar K$\alpha$ radiation in second order have been recorded in 4 ms.

The vacuum XCS has the potential for measuring ion temperature profiles in a single discharge with good time resolution. It is hoped that this instrument can be installed on TFTR in the future to aid in $T_i$ measurements and to permit an extension of the studies of spectra of high-Z highly stripped (F-, Ne-, Na-like, etc.) ions for advancement of atomic physics and in the search for suitable x-ray laser transitions.

## ACKNOWLEDGMENTS

REFERENCES


/1/ HILL, K. W., et al., "Tokamak Physics Studies Using X-Ray Diagnostic
   Methods," Proc. of Course and Workshop on Basic and Advanced Fusion Plasma
   Diagnostic Techniques, Varenna, Italy, September 1986, to be published.

/2/ HILL, K. W., BITTER, M., DIESSO, M., DUDEK, L., VON GOELER, S., HAYES,
   S., JOHNSON, L. C., KIRALY, J., MOSHEY, E., RENDA, G., SESNIC, S.,
   SAUTHOFF, N. R., TENNEY, F., and YOUNG, K. M., Rev. Sci. Instrum. 56 (May
   1985) 840.

/3/ SILVER, E. H., BITTER, M., BRAU, K., EAMES, D., GREENBERGER, A., HILL,
   K. W., MEADE, D. M., RONEY, W., SAUTHOFF, N. R., and VON GOELER, S., Rev.
   Sci. Instrum. 56 (May 1985) 1198.

/4/ VON GOELER, S., Diagnostics for Fusion Experiments, Ed. E. Sindoni and
   C. Wharton, (Pergamon, New York, 1979) 79.

/5/ VON GOELER, STEVENS, J., BERNABEI, S., BITTER, M., CHU, T. K.,
   EFTHIMION, P., FISCH, N., HOOKE, W., HILL, K., HOSEA, J., JOBES, F.,
   KARNEY, C., MERVINE, J., MESERVEY, E., MOTLEY, R., RONEY, P., SESNIC, S.,
   SILBER, K., and TAYLOR, G., Nucl. Fusion 25 (1985) 1515.

/6/ HILL, K. W., VON GOELER, S., BITTER, M., CAMPBELL, L., COWAN, R. D.,
   FRAENKEL, B., GREENBERGER, HORTON, R., HOVEY, J., RONEY, W., SAUTHOFF, N.
   R., and STODIEK, W., Phys. Rev. A19 (1979) 1770.

/7/ HILL, K. W., et al., Rev. Sci. Instrum. 56 (1985) 1165; BITTER, M., et
   al., Rev. Sci. Instrum. 57 (1986) 2145.

/8/ BARTIROMO, R., Workshop on Diagnostics for Fusion Reactor Conditions,
   Varenna, Italy, September 1982, (Pergamon, New York, 1982) 123.

/9/ KALLNE, E., KÄLLNE, J., and RICE, J. E., Phys. Rev. Lett. 49 (1982) 330.

/10/ BITTER, M., VON GOELER, S., HORTON, R., GOLDMAN, M., HILL, K. W., SAUTHOFF, N. R., and STODIEK, W., Princeton Plasma Physics Laboratory Report PPPL-1490 (1978), Phys. Rev. Lett. 42 (1979) 304.

/11/ BITTER, M., HILL, K. W., ZARNSTORFF, M., VON GOELER, S., HULSE, R., JOHNSON, L. C., SAUTHOFF, N. R., SESNIC, S., YOUNG, K. M., TAVERNIER, M., BELY-DUBAU, F., FAUCHER, P., CORNILLE, M., and DUBAU, J., Phys. Rev. A32 (1985) 3011.

/12/ HILL, K. W., BITTER, M., GOLDMAN, M., SAUTHOFF, N. R., and VON GOELER, S., Bull. Am. Phys. Soc. 26 (September 1981) 864.

/13/ WONG, K. L., BITTER, M., HAMMETT, G. W., HEIDBRINK, W., HENDEL, H.W., et al., Phys. Rev. Lett. 55 (1985) 2587.

/14/ BITTER, M., et al., Princeton Plasma Physics Laboratory Report PPPL-2357, (July 1986).

/15/ BELY-DUBAU, F., FAUCHER, P., STEEMAN-CLARK, L., BITTER, M., VON GOELER, S., HILL, K. W., CAMHY-VAL, C., and DUBAU, J., Phys. Rev. A26 (1982) 3459.

/16/ BITTER, M., VON GOELER, S., COHEN, S.A., HILL, K. W., SESNIC, S., TENNEY, F., TIMBERLAKE, J., SAFRONOVA, U. I., VAINSHTEIN, L. A., DUBAU, J., LOULERGUE, M., BELY-DUBAU, F., and STEENMAN-CLARK, L., Phys. Rev. A29 (1984) 661.

/17/ BEIERSDORFER, P., BITTER, M., VON GOELER, S., COHEN, S., HILL, K. W., TIMBERLAKE, J., WALLING, J. R. S., CHEN, M. H., HAGELSTEIN, P. L., and SCOFIELD, J. H., Princeton Plasma Physics Laboratory Report PPPL-2322 (April, 1986), Phys. Rev. A34 (1986) 1297.

/18/ BELY-DUBAU, F., BITTER, M., DUBAU, J., FAUCHER, P., GABRIEL, A. H., HILL, K. W., VON GOELER, S., SAUTHOFF, N. R., and VOLONTE, S., Phys. Lett. 93A (1983) 189.

/19/ RICE, J. E., MARMAR, E. S., TERRY, J. L., KÄLLNE, and J. KÄLLNE, Phys. Rev. Lett. 56 (1986) 50.

/20/ HILL, K. W., VON GOELER, S., BITTER, M., DAVIS, W., DUDEK, L., FREDD, E., JOHNSON, L. C., KIRALY, J., MCGUIRE, K., MONTAGUE, J., MOSHEY, E., SAUTHOFF, N. R., and YOUNG, K. M., Rev. Sci. Instrum. 56 (1985) 830.

/21/ PETRASSO, R., GERASSIMENKO, M., SEGUIN, F. H., TING, J., KROGSTAD, R., GAUTHIER, P., HAMILTON, W., RAMSEY, A. T., BURSTEIN, P., and GRANETZ, R., Rev. Sci. Instrum. 51 (1980) 585.

/22/ MCGUIRE, K., COLCHIN, R.J., FREDRICKSON E., HILL, K.W., JOHNSON, L.C., MORRIS, W., PARE, V., SAUTHOFF, N.R. and VON GOELER, S., Rev. Sci. Instrum. 57 (1986) 2136.

/23/ KIRALY, J., BITTER, M., GOELER VON S, HILL, K.W., JOHNSON, L.C., MCGUIRE, K., SESNIC,S., SAUTHOFF, N.R., TENNEY, F. and YOUNG, K.M. Rev. Sci.Instrum. 51 (May 1985) 827.

/24/ KIRALY, J.,BITTER, M., EFTHIMION, P.C., VON GOELER, S., GREK, B., HILL, K.W., JOHNSON, D.W., MCGUIRE, K., SAUTHOFF, N.R., SESNIC, S., STAUFFER, F.J., TAIT, G.D., and TAYLOR, G., Princeton Plasma Physics Laboratory Report PPPL-2254 (September 1986).

/25/ BRAU, K., GOELER, VON S., BITTER, M., COWAN, R.D., EAMES, D., HILL, K.W.,SAUTHOFF, N.R., SILVER, E., STODIEK, W., Princeton Plasma Physics Laboratory Report PPPL-1644 (March 1980); Phys. Rev. A22 (1980) 2769.

/26/ ENGELHARDT, W., et al., in Proc. 7th Internat. Conf., Plasma Physics and Controlled Nuclear Fusion Research, Innsbruck, 1978, IAEA-CN/37/Vienna, 1979, Vol. 1, 123.

/27/ BOYD, D., CAVALLO, A., COHEN, S., VON GOELER, S., HULSE, R., MANOS, D., SMITH, R., Plasma Physics and Controlled Fusion, Vol. 27, No. 3, 229-243, 1985.

/28/ PETRASSO, R.D., WENZEL, K.W., HOPF, J.E., SIGMAR, D.J., GREENWALD, M.,
     TERRY, J.L. and PARKER, J., Phys. Rev. Lett. 57 (1986) 707.

/29/ FONCK, R., et al., Princeton Plasma Physics Laboratory Report PPPL-2374.

/30/ GOELER, VON S., HILL, K.W., BITTER, M., CLIFFORD, C., FREDD, E.,
     GOLDMAN, M., JOHNSON, L.C., KU, L.P., MOSHEY, E., RENDA, G. SAUTHOFF,
     N.R., SESNIC, S., TENNEY, F.H., and YOUNG, K.M., Proc. of Course on
     Diagnostics for Fusion Reactor Conditions, Varenna, Italy, 1982 (Pergamon,
     New York, 1982), Vol. 1, 69.

/31/ LIEW, S. L., KU, L.P., KOLIBAL, J., HILL, K.W., Fusion Technol. 8 #1,
     (July 1985) 1020.

/32/ SHIMADA, M., et al., General   ...ic Report., GA-A16186 (1981).

/33/ HILL, K.W., BITTER, M., GOELER, VON S., HIROE, S., HULSE, R., RAMSEY,
     A.T., SESNIC, S., SHIMADA, M., and STRATTON, B.C.,Rev. Sci. Instrum. 57
     (1986) 2151.

/34/ BELY DUBAU, F, DUBAU, J., FAUCHER, P., GABRIEL, A.H., Mon. Not. R.
     Astron. Soc. 198 (1982) 239.

/35/ SESNIC, S., BITTER, M., HILL, K.W., HIROE, S., HULSE, R., SHIMADA, M.,
     STRATTON, B.C., and GOELER, VON S., Rev. Sci. Instrum. 57 (1986) 2148.

/36/ GOULDING, F.S., LANDIS, D.A., MADDEN, N.W, IEEE Trans. Nucl. Sci. NS-30
     (1983) 301.

/37/ BRETZ, N.L., et al., Princeton Plasma Physics Laboratory Report MATT-
     1077 (1974).

/38/ BITTER, M., et al., Rev. Sci. Instrum. 57 (1986) 2145.

/39/ BOIE, R.A., et al., Nucl. Instrum. Methods 201 (1982) 93.

/40/ PLATZ, R., et al., Association EURATOM-CEA Report EUR-CEA-FC 1057
     (1980).

/41/ HOBBY, M.G., PEACOCK, N.J., BATEMAN, J.E., Culham Laboratory Report CLM-R203 (1980).

/42/ GABRIEL, A.H., Mon. Not. R. Astron. Soc. 160 (1972) 99.

/43/ FREDRICKSON, E., et al., Nucl. Fusion 26 (1986) 849.

/44/ STEVENS, J., et al., Nucl. Fusion 25 (1985) 1529.

/45/ VON GOELER, S., et al., Proc. of Course on Diagnostics for Fusion Reactor Conditions (Varenna, Italy) September 1982 (Pergamon, New York, 1983) Vol. I, 87.

/46/ KU, L.P., "Nuclear Radiation Analysis for TFTR," Princeton Plasma Physics Laboratory Report PPPL-1711, September (1980).

/47/ ENGLE, W.W. Jr., "ANISN - A One-Dimensional Discrete Ordinates Transport Code with Anisotropic Scattering," CCC-254, Radiation Shielding Information Center, Oak Ridge, TN (1973).

/48/ KUCKUCK, R.W., "Semiconductor Detectors for use in the Current Mode," Lawrence Livermore National Laboratory Report No. UCRL-51011.

/49/ IQCODE, a transport-response computer code from T. Jordan of Experimental and Mathematical Physics Consultants, Box 66331, Los Angeles, CA 90066 (Private Communication).

/50/ JOHNSON, L.C., et al., Rev. Sci. Instrum. 57 (1986) 2133.

/51/ FRANCO, E.D. and BOYLE, M.J., in Applications of Thin Film Multilayered Structures to Figured X-Ray Optics, SPIE (1985) Vol. 563, 354.

/52/ UNDERWOOD, J.H., and BARBEE, T.W. JR., in Low Energy X-Ray Diagnostics, AIP Conf. Proceedings No. 75, Ed. D.R. Attwood and B.L. Henke (American Institute of Physics, New York, 1981) 170.

/53/ VON GOELER, S., "X-Ray Spectroscopy on Tokamaks," Proc. of Course on Diagnostics for Fusion Reactor Conditions, Varenna, Italy, September 1982, (Pergamon, New York, 1983) Vol. I, 109.

FIGURE CAPTIONS


Fig. 1    (a) Soft x-ray spectrum from the central chord of TFTR measured by

         the x-ray pulse-height-analysis (PHA) diagnostic.  (b) Expanded view

         of iron Kα spectrum from PLT measured by x-ray crystal spectrometer

         (XCS) with resolving power. (E/ΔE) of 1700.  (c) Further expansion

         of Fe Kα spectrum from PLT measured with XCS having a resolving power

         of 15,000.


Fig. 2    Excitation rates for several charge states of iron multiplied by

         fractional abundance according to coronal equilibrium /33/.  Fe 25 is

         $FE^{+24}$.


Fig. 3    Schematic of horizontal x-ray PHA on TFTR illustrating array of six

         detectors, remotely selectable foil and aperture arrays, and neutron

         and gamma-ray shielding.


Fig. 4    Schematic illustrating principle of Bragg x-ray crystal spectrometer

         (XCS).


Fig. 5    Schematic of horizontal x-ray imaging system (XIS) on TFTR showing

         detector and preamplifier arrays, selectable foil ladders, viewing

         slot, and radiation shielding.

Fig. 6   Model for interpreting XIS data.  (a) Contours of equal emissivity decreasing towards edge, showing m = 1 magnetic island.  (b) Emissivity profile showing flattening at m = 1 island.  (c) and (d) Comparison of simulated signal from several chords to measured XIS data.

Fig. 7   Forward peaked bremsstrahlung emission intensity contours for mildly relativistic electrons.

Fig. 8   Schematic of collimated hard x-ray detector used to measure angular distribution of bremsstrahlung spectra from PLT.

Fig. 9   Hard x-ray spectrum from PLT measured at $\theta = 28°$ toward the forward direction.  The experimental points are fitted by a "two temperature" fit consisting of the sum of two exponential functions.

Fig. 10  Calculated angular dependence of photon counts for $h\nu = 100$ and $300$ keV.  Various dashed curves represent a ± 50% change in one model parameter ($T_{HF}$, $\Sigma_{\perp}$, or $T_{HB}$) relative to those values shown on the solid curve, with the other parameters remaining fixed.

Fig. 11  XIS background noise, resulting from TFTR fusion neutron emission (and secondary gamma rays), versus shield thickness.  The three-dimensional model agrees with measurements for a 2.5-cm-thick lead shield.  One-dimensional models overestimate the noise.

Fig. 12  Background counts in PHA Si(Li) detector resulting from fusion neutrons and secondary radiation versus shield thickness.  One-dimensional slab and spherical models overpredict measured counts.
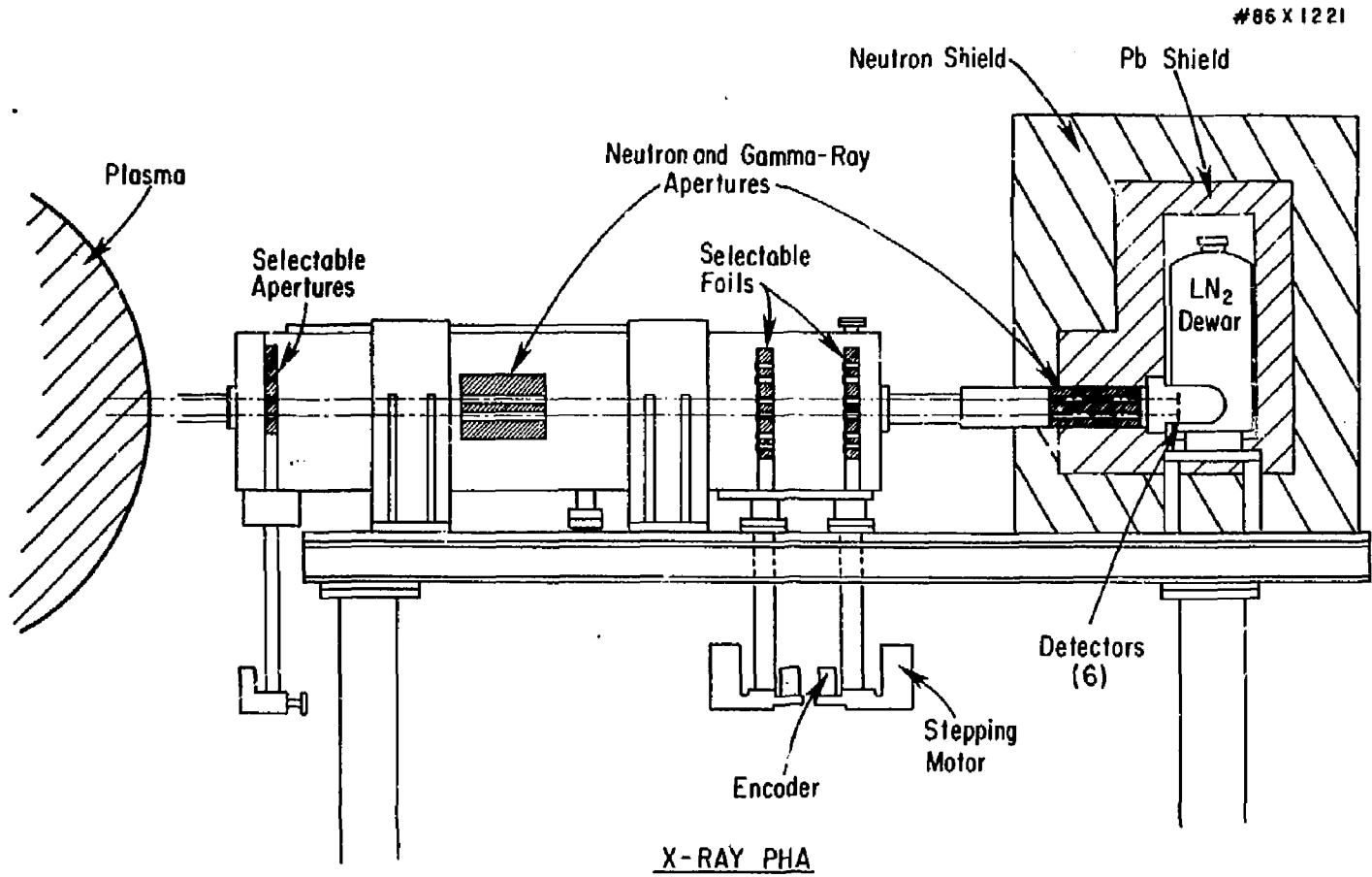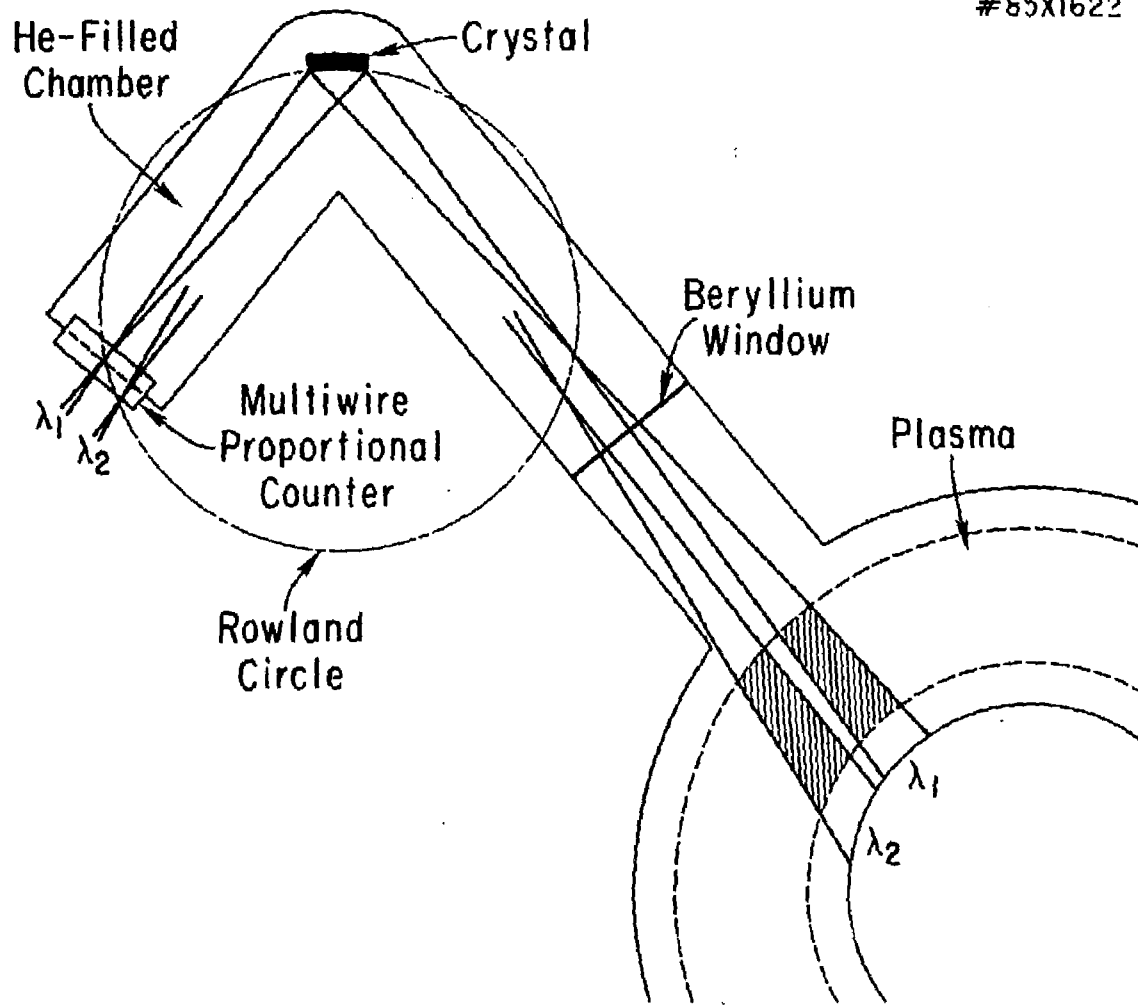
Fig. 1.

Fig. 2.

X-RAY PHA

Fig. 3.

He-Filled Chamber

Crystal

Beryllium Window

Plasma

$\lambda_1$
$\lambda_2$

Multiwire Proportional Counter

Rowland Circle

$\lambda_1$
$\lambda_2$

Fig. 4.

PF Coils
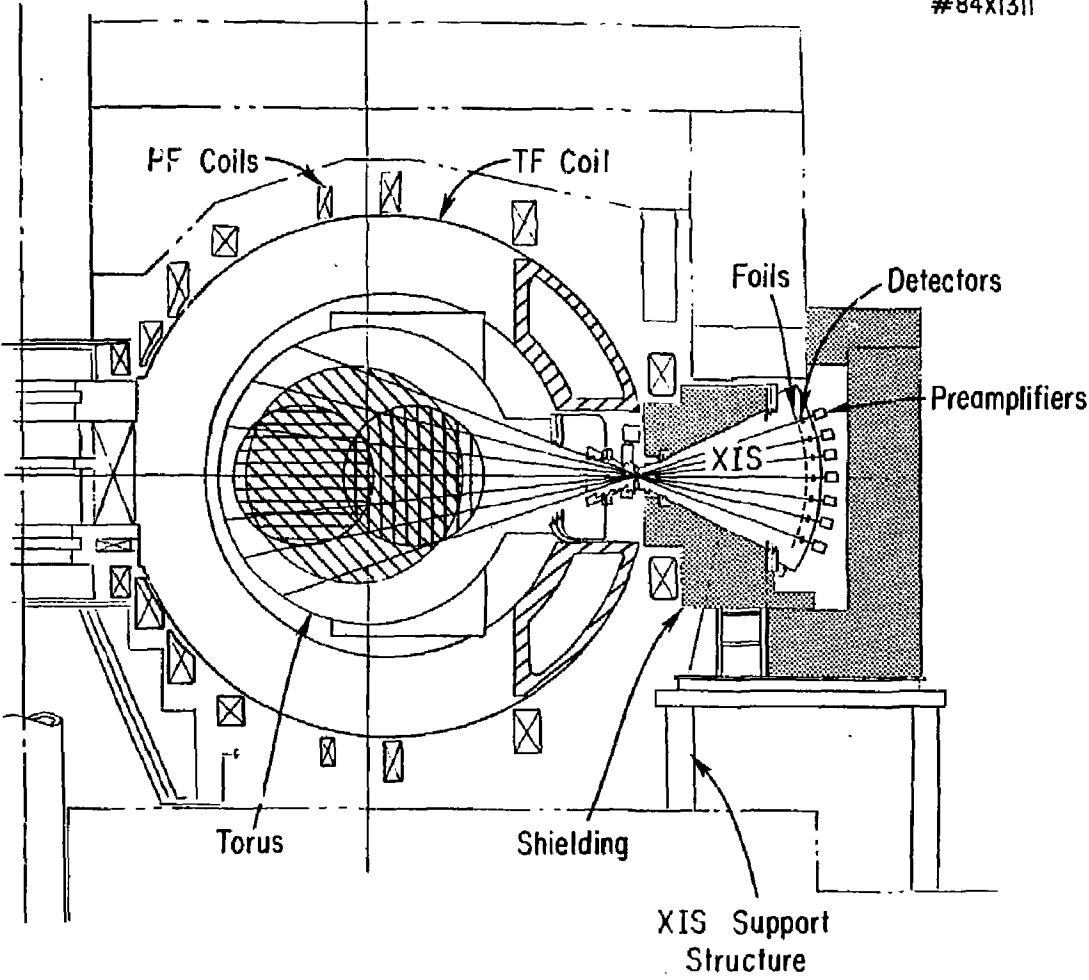
TF Coil

Foils

Detectors

Preamplifiers

XIS

Torus

Shielding

XIS Support
Structure
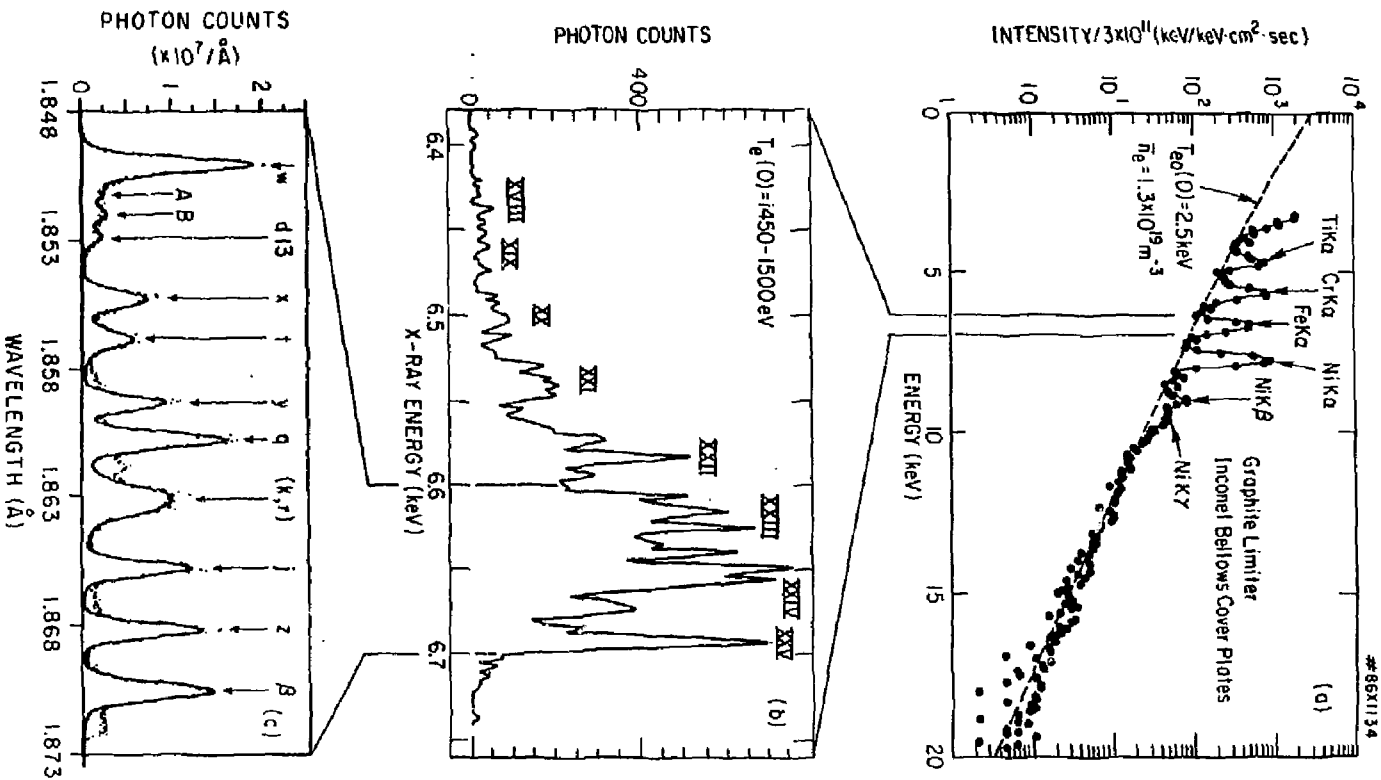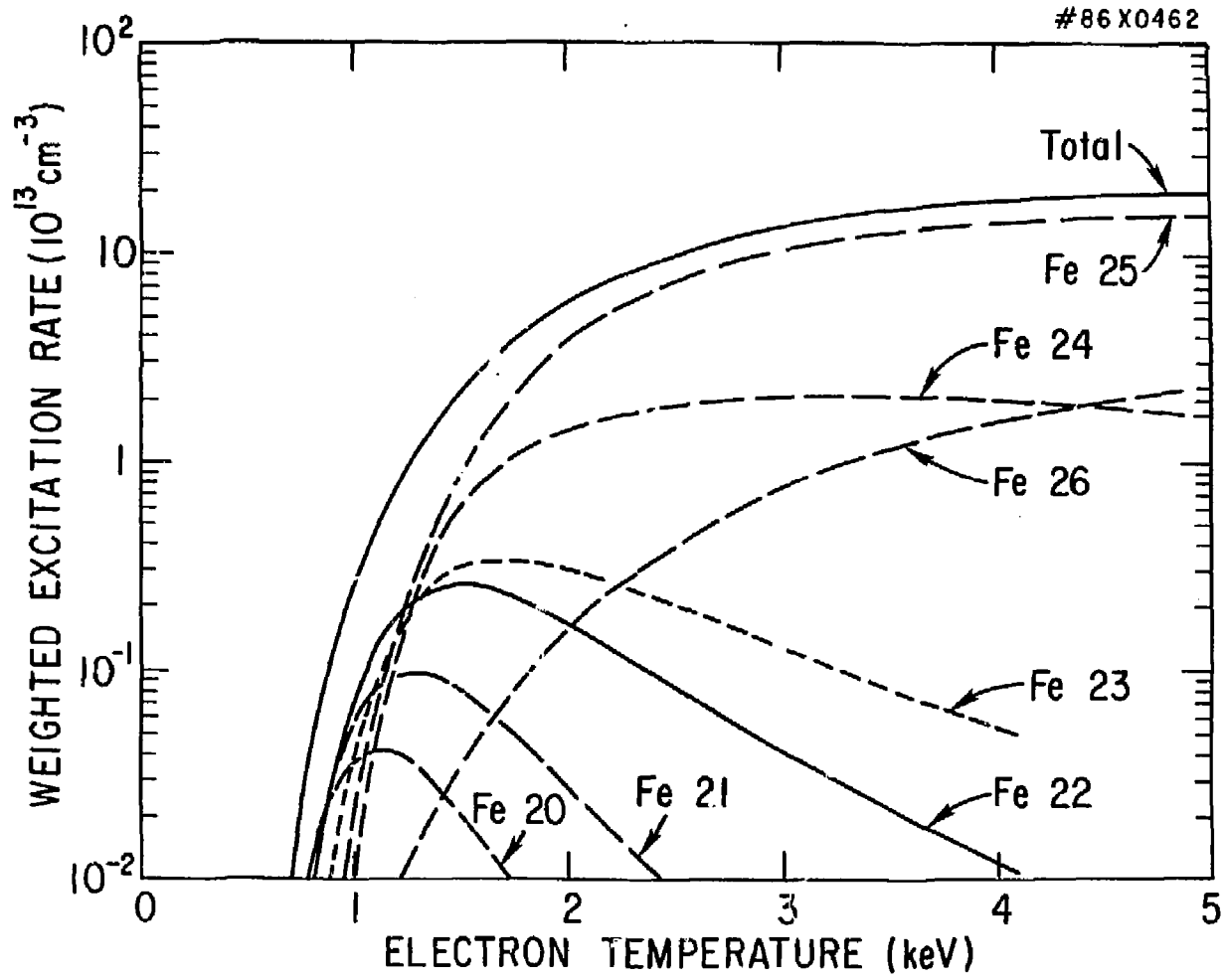
Fig. 5.
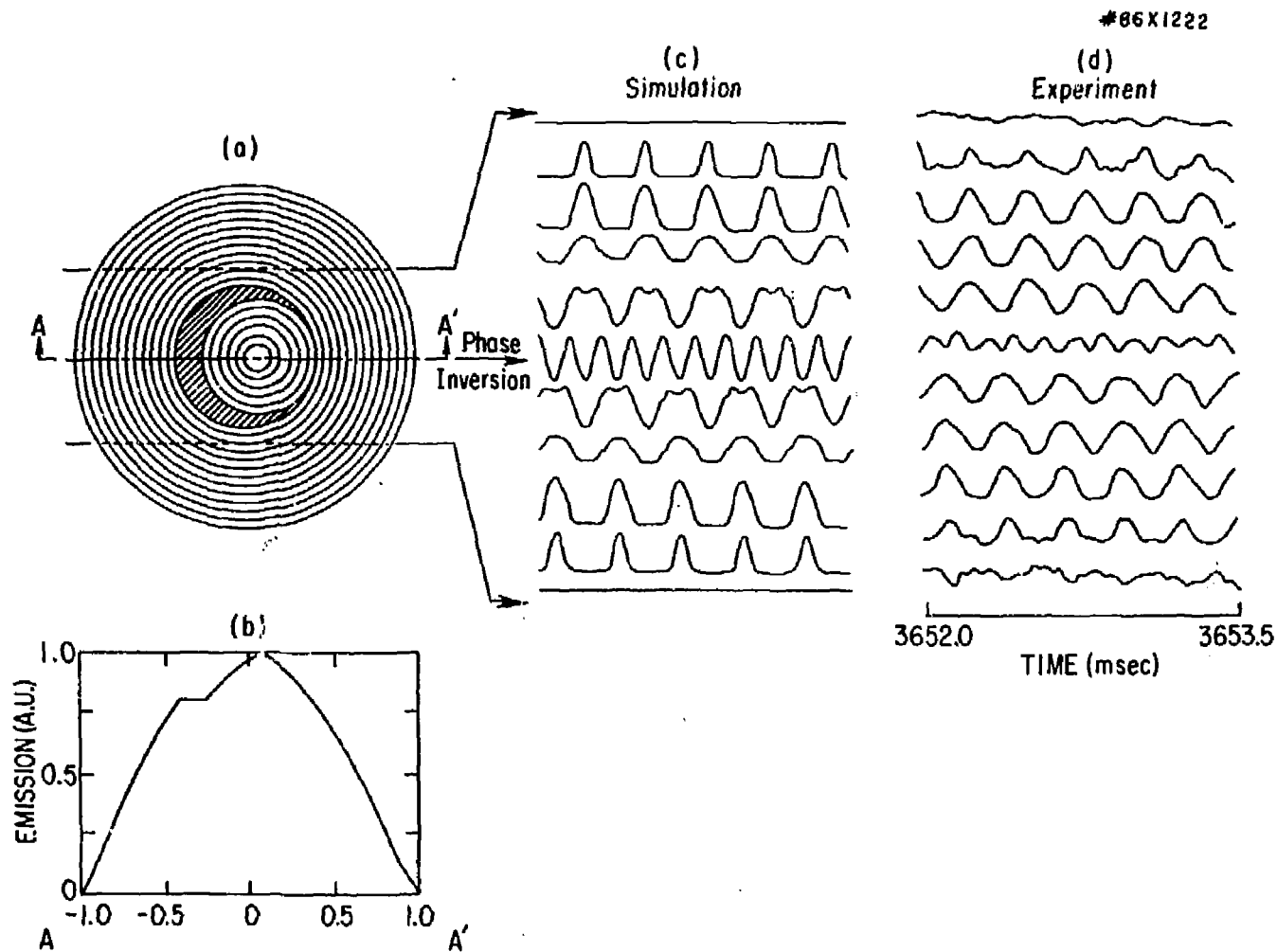
Fig. 6.
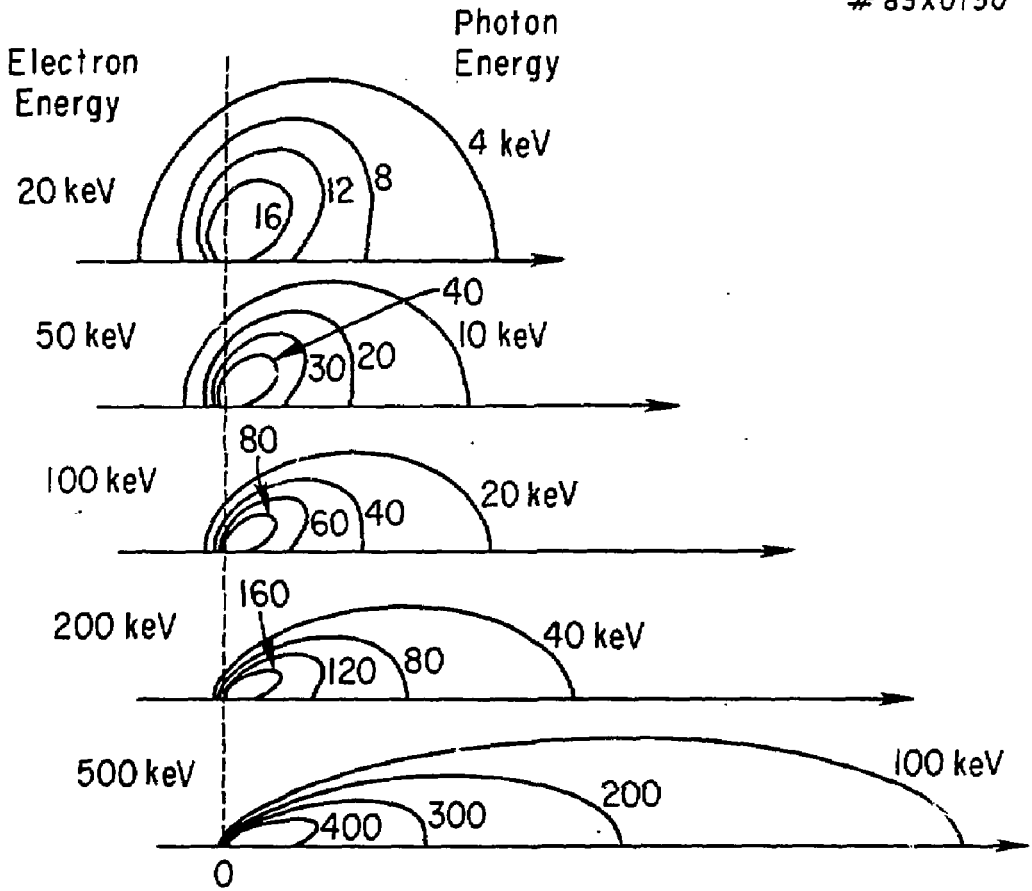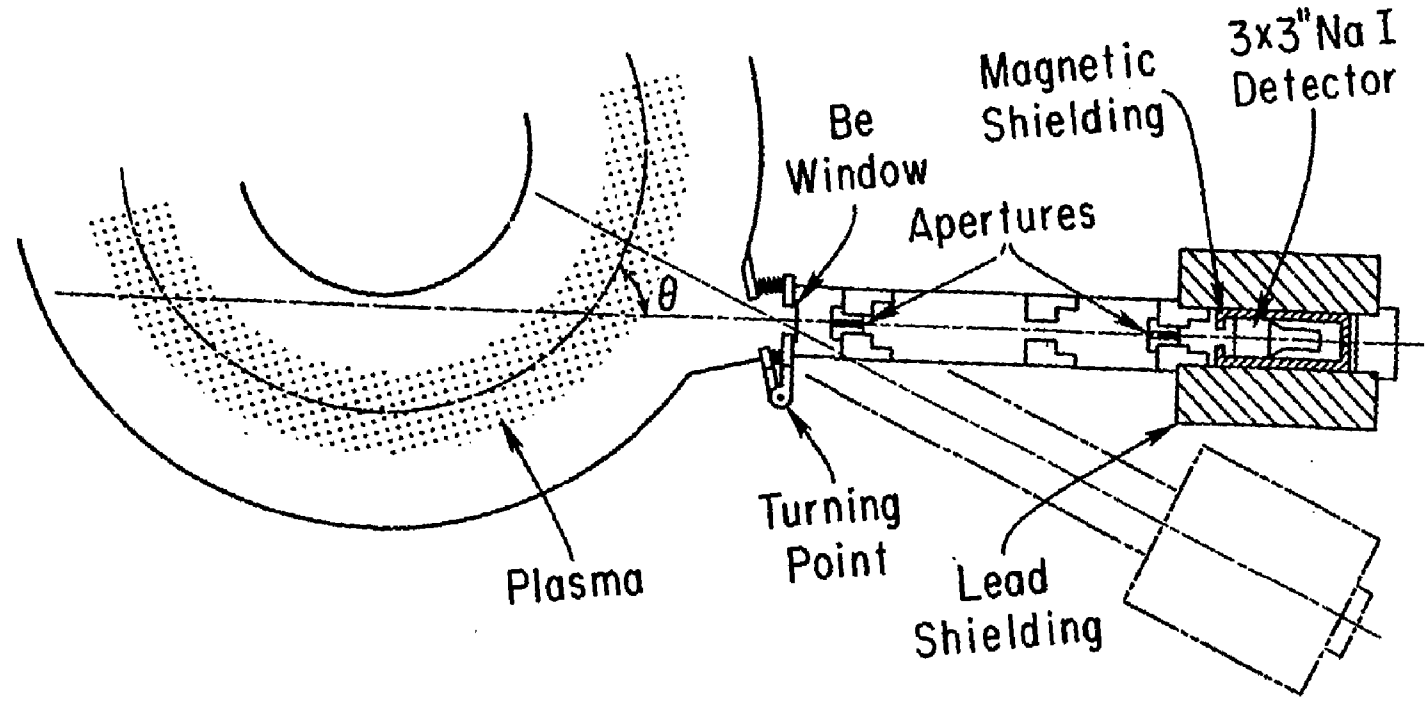
Fig. 7.

# TANGENTIAL DETECTOR
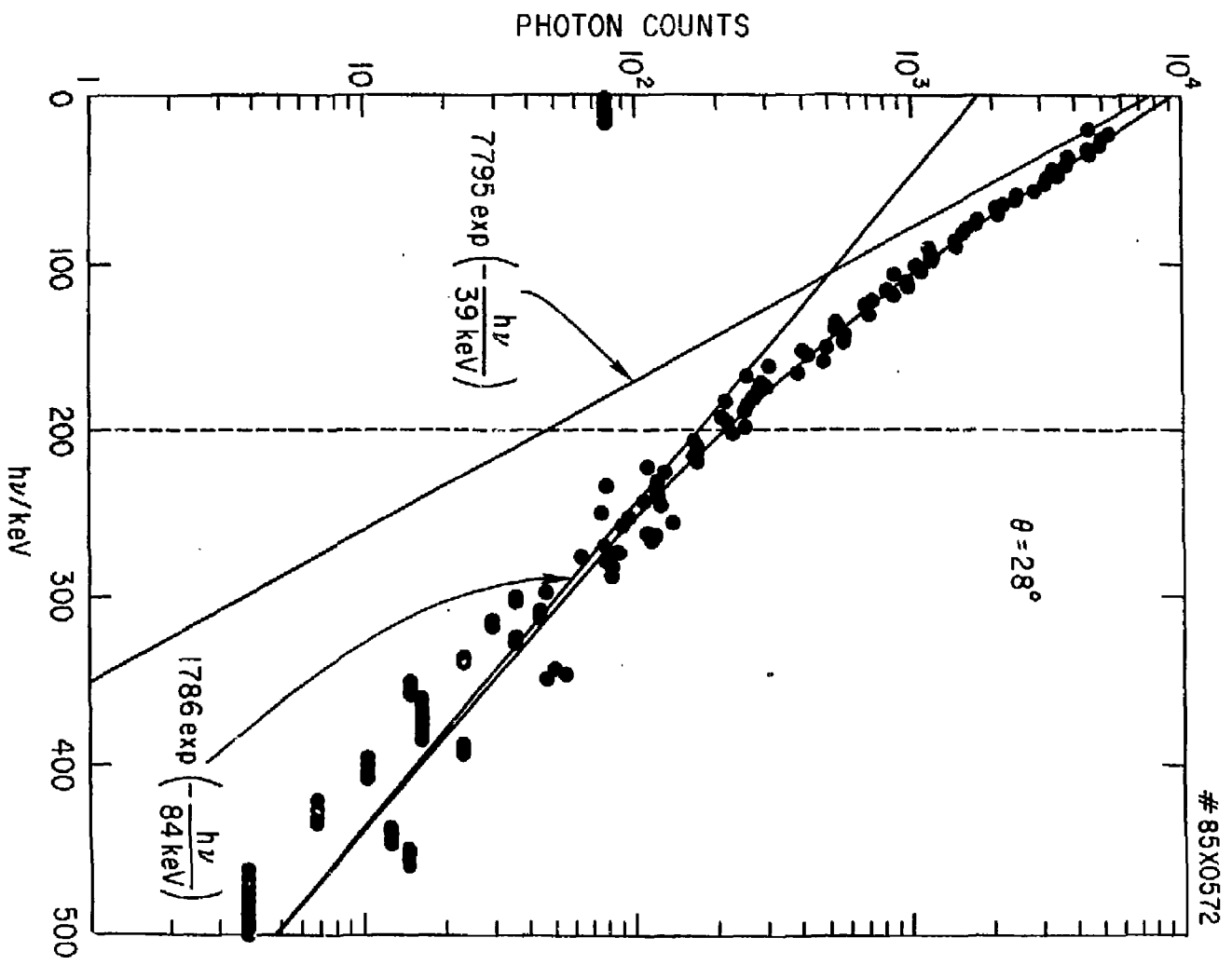


Fig. 8.

Fig. 9.

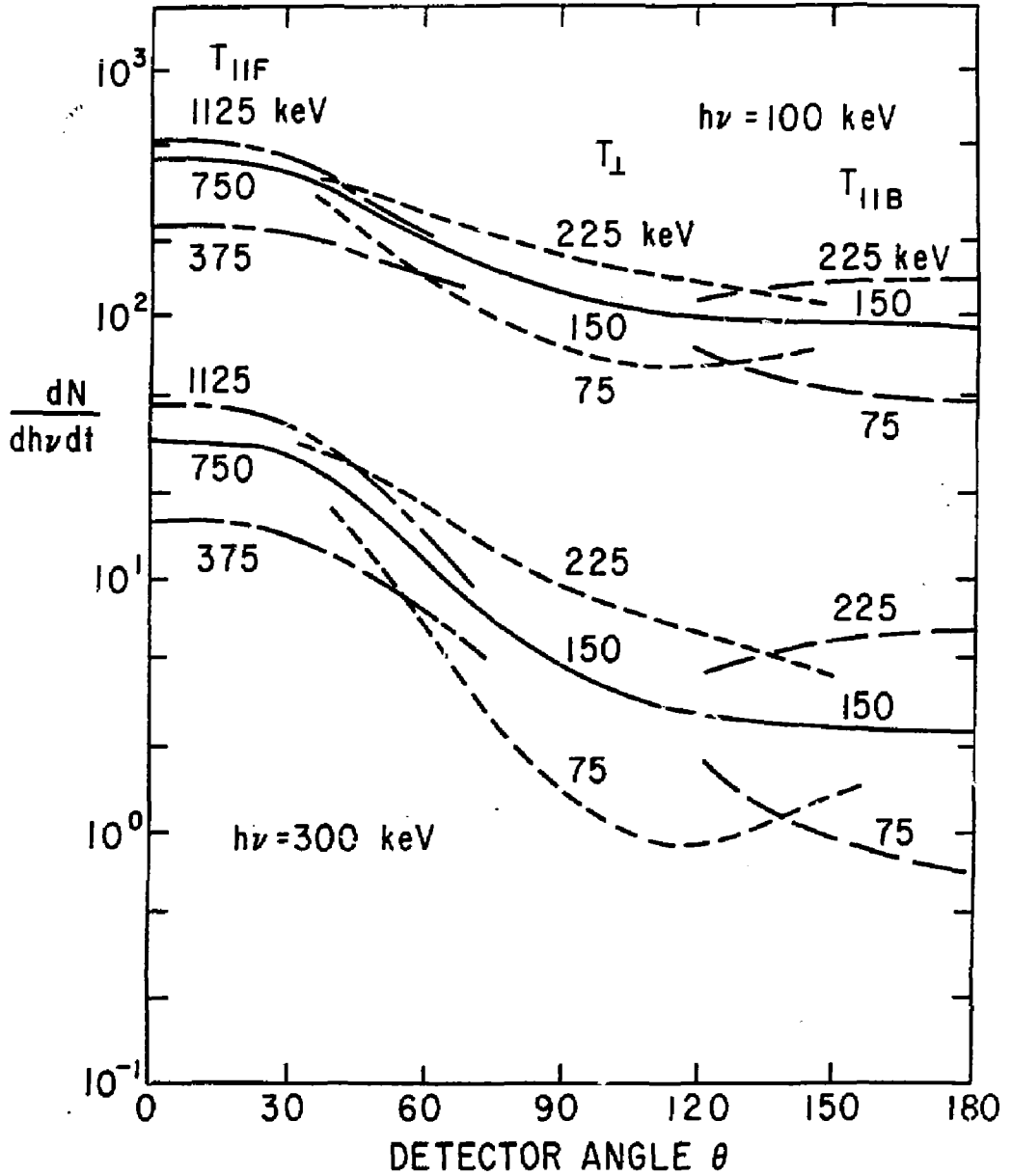Fig. 10.

#86X1219



SPECIFIC DETECTOR CURRENT $(\frac{nA}{neutron/s})$

SHIELD THICKNESS (cm)

Fig. 11.

#86XI185
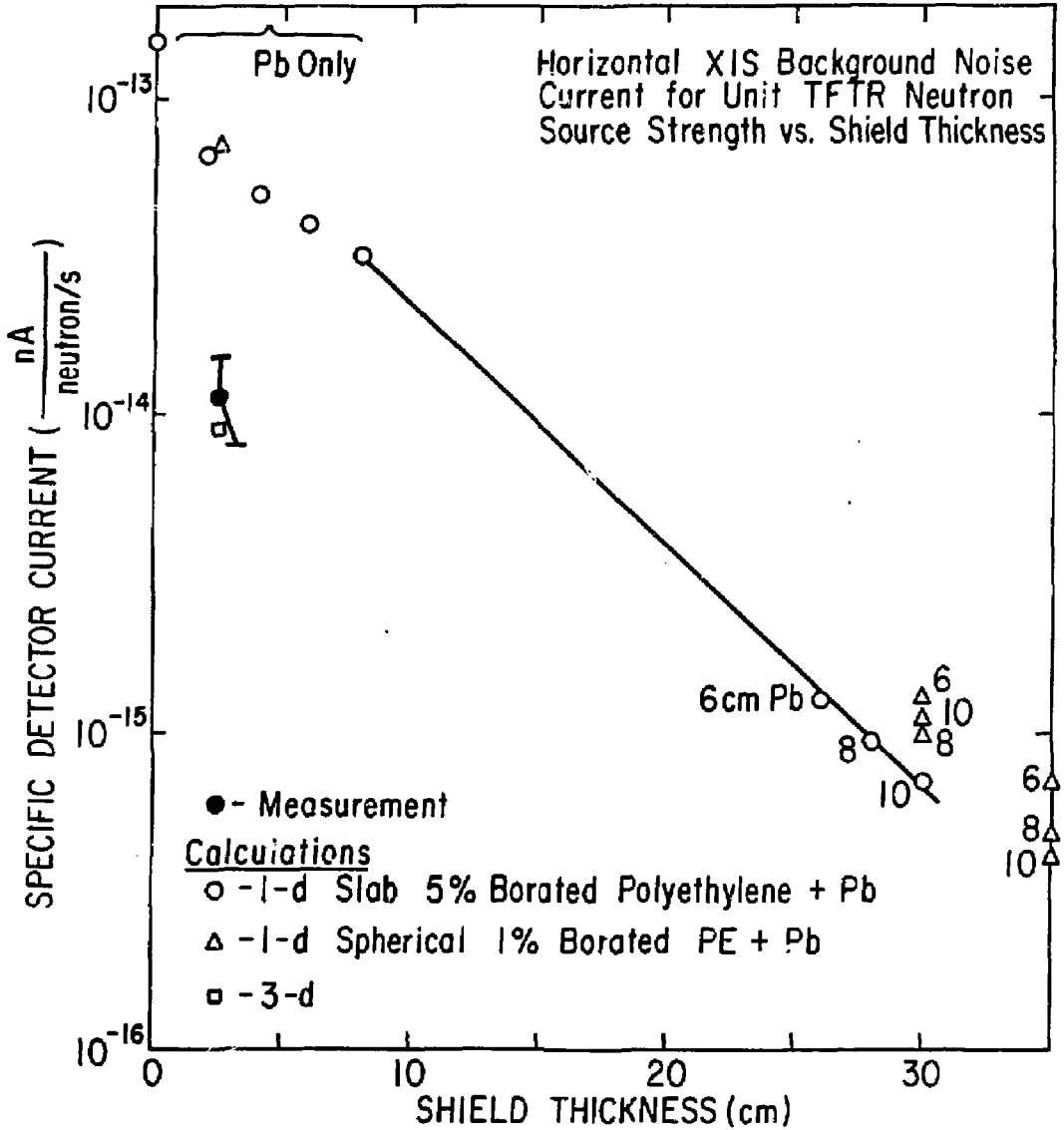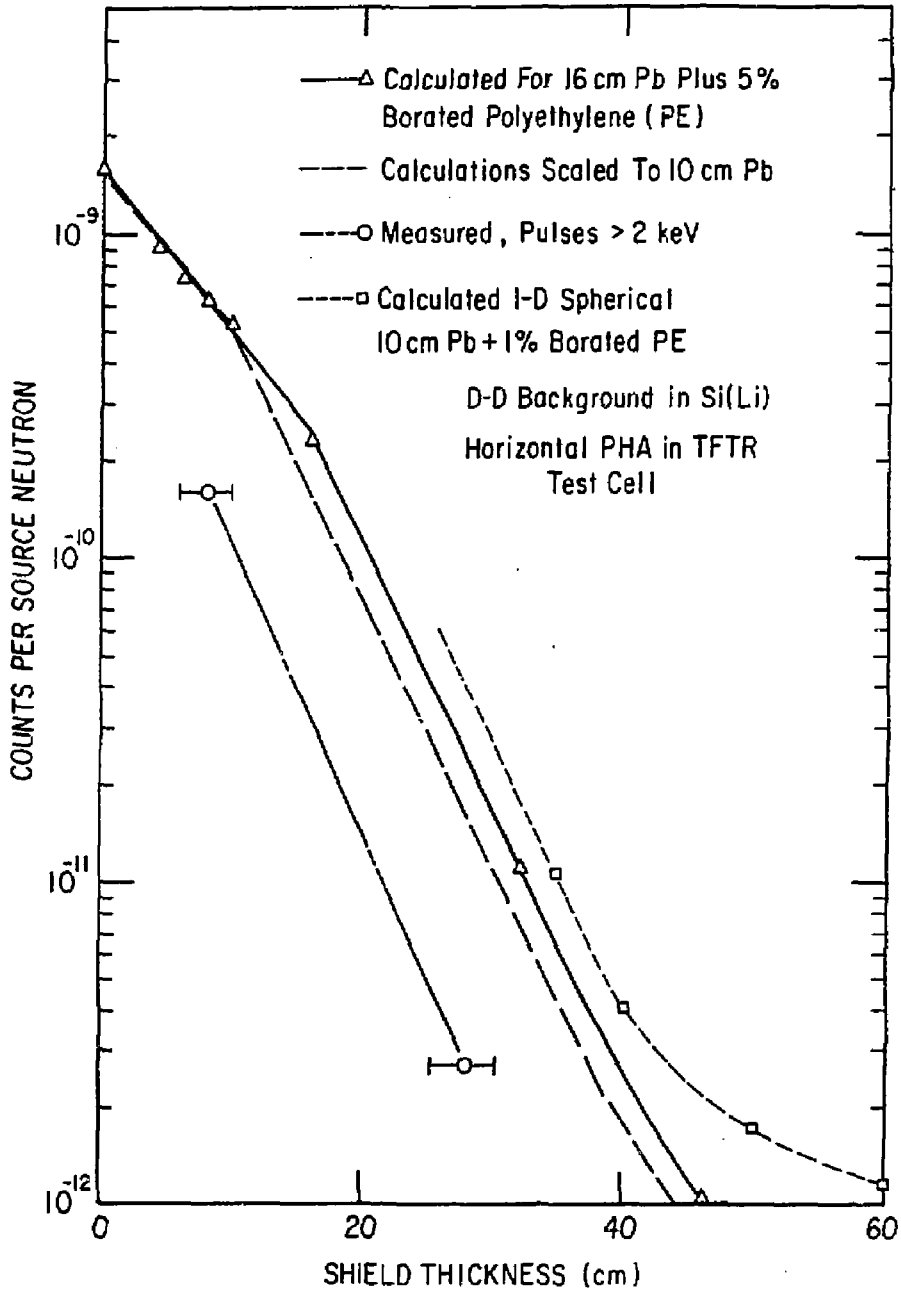


Fig. 12.

Dr. Frank J. Paoloni, Univ of Wollongong, AUSTRALIA
Prof. M.H. Brennan, Univ Sydney, AUSTRALIA
Plasma Research Lab., Australian Nat. Univ., AUSTRALIA
Prof. I.R. Jones, Flinders Univ., AUSTRALIA
Prof. F. Cap, Inst Theo Phys, AUSTRIA
Prof. M. Heindler, Institut fur Theoretische Physik, AUSTRIA
M. Goossens, Astronomisch Instituut, BELGIUM
École Royale Militaire, Lab de Phys Plasmas, BELGIUM
Com. of European, Dg XII Fusion Prog, BELGIUM
Prof. R. Boucique, Laboratorium voor Natuurkunde, BELGIUM
Dr. P.H. Sakanaka, Univ Estadual, BRAZIL
Instituto De Pesquisas Espaciasi-INPE, BRAZIL
Library, Atomic Energy of Canada Limited, CANADA
Dr. M.P. Bachynski, MPB Technologies, Inc., CANADA
Dr. H.M. Skarsgard, Univ of Saskatchewan, CANADA
Dr. H. Barnard, University of British Columbia, CANADA
Prof. J. Teichmann, Univ. of Montreal, CANADA
Prof. S.R. Sreenivasan, University of Calgary, CANADA
Prof. Tudor W. Johnston, INRS-Energie, CANADA
Dr. C.R. James, Univ. of Alberta, CANADA
Dr. Peter Lukac, Komenskeho Univ, CZECHOSLOVAKIA
The Librarian, Culham Laboratory, ENGLAND
Mrs. S.A. Hutchinson, JET Library, ENGLAND
C. Mouttet, Lab. de Physique des Milieux Ionises, FRANCE
J. Radet, CEN/CADARACHE - Bat 506, FRANCE
Dr. Tom Mual, Academy Bibliographic, HONG KONG
Preprint Library, Cent Res Inst Phys, HUNGARY
Dr. B. Dasgupta, Saha Inst, INDIA
Dr. R.K. Chhajlani, Vikram Univ. INDIA
Dr. P. Kaw, Institute for Plasma Research, INDIA
Dr. Phillip Rosenau, Israel Inst Tech, ISRAEL
Prof. S. Cuperman, Tel Aviv University, ISRAEL
Librarian, Int'l Ctr Theo Phys, ITALY
Prof. G. Rostagni, Univ Di Padova, ITALY
Miss Cielia De Paio, Assoc EURATOM-ENEA, ITALY
Biblioteca, del CNR EURATOM, ITALY
Dr. H. Yamato, Toshiba Res & Dev, JAPAN
Prof. I. Kawakami, Atomic Energy Res. Institute, JAPAN
Prof. Kyoji Nishikawa, Univ of Hiroshima, JAPAN
Direc. Dept. Lg. Tokamak Res. JAERI, JAPAN
Prof. Satoshi Itoh, Kyushu University, JAPAN
Research Info Center, Nagoya University, JAPAN
Prof. S. Tanaka, Kyoto University, JAPAN
Library, Kyoto University, JAPAN
Prof. Nobuyuki Inoue, University of Tokyo, JAPAN
S. Mori, JAERI, JAPAN
M.H. Kim, Korea Advanced Energy Research Institute, KOREA
Prof. D.I. Choi, Adv. Inst Sci & Tech, KOREA
Prof. B.S. Liley, University of Waikato, NEW ZEALAND
Institute of Plasma Physics, PEOPLE'S REPUBLIC OF CHINA
Librarian, Institute of Phys, PEOPLE'S REPUBLIC OF CHINA
Library, Tsing Hua University, PEOPLE'S REPUBLIC OF CHINA

Z. Li, Southwest Inst. Physics, PEOPLE'S REPUBLIC OF CHINA
Prof. J.A.C. Cabral, Inst Superior Tecn, PORTUGAL
Dr. Octavian Petrus, AL I CUZA University, ROMANIA
Dr. Johan de Villiers, Plasma Physics, AEC, SO AFRICA
Prof. M.A. Hellberg, University of Natal, SO AFRICA
Fusion Div. Library, JEN, SPAIN
Dr. Lennart Stenflo, University of UMEA, SWEDEN
Library, Royal Inst Tech, SWEDEN
Prof. Hans Wilhelmson, Chalmers Univ Tech, SWEDEN
Centre Phys des Plasmas, Ecole Polytech Fed, SWITZERLAND
Bibliotheek, Fom-Inst Voor Plasma-Fysica, THE NETHERLANDS
Dr. D.D. Ryutov, Siberian Acad Sci, USSR
Dr. G.A. Eliseev, Kurchatov Institute, USSR
Dr. V.A. Glukhikh, Inst Electro-Physical, USSR
Dr. V.T. Tolok, Inst. Phys. Tech. USSR
Dr. L.M. Kovrizhnykh, Institute Gen. Physics, USSR
Prof. T.J.M. Boyd, Univ College N Wales, WALES
Nuclear Res. Establishment, Julich Ltd., W. GERMANY
Bibliothek, Inst. Fur Plasmaforschung, W. GERMANY
Dr. K. Schindler, Ruhr Universitat, W. GERMANY
ASDEX Reading Rm, IPP/Max-Planck-Institut fur
  Plasmaphysik, W. GERMANY
Librarian, Max-Planck Institut, W. GERMANY
Prof. R.K. Janev, Inst Phys, YUGOSLAVIA